UNIVERSIDAD INTERNACIONAL DE VALENCIA

MASTER IN ASTRONOMY AND ASTROPHYSICS
ACADEMIC YEAR 2023-2024

*SEGUNDA CONVOCATORIA*

# Interstellar Interceptors. Mission design for rendezvous with objects in hyperbolic orbits.

JORGE MARTÍNEZ GARRIDO

SUPERVISED BY:

JOSEP M. TRIGO-RODRÍGUEZ (ICE-CSIC/IEEC)
ELOY PEÑA-ASENSIO (POLITECNICO DI MILANO)

APRIL, 2024

MADRID, SPAIN

# Abstract

The discovery of interstellar objects opens a new window to study asteroids and comets formed in other planetary systems. Their highly eccentric orbits challenge our ability to reach these bodies, but the giant scientific return well requires all our efforts. In this work a deep dynamic analysis on the most suitable transfer orbits to the two first identified interstellar interlopers: 1I/'Oumuamua and 2I/Borisov is presented. The analysis exemplifies the intrinsic difficulty behind the development of dedicated missions to intercept these bodies. By analyzing different launch scenarios, porkchop plots for the specific energy at launch are generated for both prograde and retrograde transfers. In addition, isolines for the total time of flight and the velocity at arrival are computed for a big span of launch and arrival dates. The entire study allows for the finding of the lowest energy transfer orbits, key to plan and develop future missions to other discovered extrasolar objects. Different launch possibilities are explored: from Earth, Lagrange point L2, or other gravity assisted maneuvers. To catch a future visitor a preferred scenario arises: using the L2 point to quickly release a rendezvous mission able to study it during close approach. The results obtained in this work are consistent with those found by other proposed missions, like the Comet Interceptor, showing that L2 is a good starting point for launching missions to intercept interstellar visitors. By parking a spacecraft at this point, more reaction time is gained to plan an optimum transfer trajectory. This is evinced by the fact that the optimum transfer takes place before the interlopers were discovered. As a direct outcome of this work the most favourable approach is a direct transfer between this Lagrange point and the discovered interstellar interloper unless ideal conditions for a gravity-assisted maneuver are met.

**Keywords:** Interstellar interlopers, transfer orbits, porkchop plots, Lagrange points, gravity-assisted maneuvers, interstellar missions, surveillance research, mission design, celestial exploration

# Contents

# List of Figures

# List of Tables

# 1 Introduction

The initial chapter is dedicated to introducing fundamental concepts pertinent to the addressed problem, delineating the various methodologies employed and outlining the objectives attained. These components serve to enhance the reader's comprehension of the project's framework. Furthermore, the concluding sections offer a compilation of real-world applications alongside a concise socioeconomic evaluation, aiming to substantiate the contemporary relevance and significance of the problem at hand.

## 1.1 Problem description and motivation

The discovery of interstellar objects such as 1I/'Oumuamua and 2I/Borisov within our solar system has ignited a surge of curiosity and scientific interest. These sub-kilometer-sized visitors, originating from distant stellar systems, present a unique opportunity to study extraterrestrial bodies that have traversed vast cosmic distances. Therefore, the main motivations behind the study of these objects are:

- **Better understanding the formation of planetary systems.** Interstellar objects can provide insights into the formation and dynamics of planetary systems beyond our own. This could help to confirm or reject the Nebular hyphotesis, which is the most popular model proposed for the formation of planetary systems by in situ measurements of the isotopic signatures.

- **Exploring the origins of life.** Analyzing the composition of interstellar objects could provide valuable information about the chemical and physical conditions present in other planetary systems, shedding light on the origins of life in the universe, which could support or reject the panspermia hyphotesis.

- **Technological innovation.** By pushing the technological boundaries of space exploration, missions to intercept interstellar objects could lead to the development of new propulsion systems and spacecraft capable of reaching unprecedented speeds and distances.

Given their exceptionally high eccentricities, heliocentric velocities, and fleeting passage

through the planetary region, there is a pressing need for the development of ready-to-launch missions capable of intercepting them.

However, the design of such missions is not straightforward. The high velocities of these objects, combined with their limited observation windows, make it difficult to accurately predict their trajectories and plan for rendezvous within the short timeframes available.

This problem presents the main motivation of this work: **devising mission orbits capable of intercepting interstellar objects**.

This research stems from the desire to unlock the mysteries surrounding these enigmatic interstellar travelers, gathering invaluable data or even returning samples from their surfaces. This pursuit not only promises to broaden our understanding of celestial dynamics and planetary formation but also holds profound implications for the future of space exploration and our comprehension of the broader universe.

## 1.2 Objectives and goals

The main objetive of this project is to design suitable targeting orbits for interstellar ojects. To achieve this purpose, the whole process is divided into the following key objectives:

- **Research on interstellar objects.** The definition of interstellar object is presented together with the official IAU nomenclature. The only two discovered objects, 1I/'Oumuamua and 2I/Borisov, are presented together with their main characteristics. The importance of the solar apex is explained too.

- **Revisiting targeting orbits.** Lambert's problems is revisited. Porkchop plots are presented to the reader together with other useful mission design tools. These are applied to the two discovered interstellar objects, demonstrating the targeting challenges considering nowadays technologies.

- **Alternate targeting orbits** Once the direct transfer problems have been introduced, the concept of Lagrangian points is presented. The analysis focuses on point L2, due to its capabilities and advantages. The gravity assist technique is revisited and explored.

- **Performance comparison.** A comparison between direct transfers and multiple flyby orbits is performed. Mission contrains including velocity impulse, time of flight, arrival excess velocity, and existing propulsive technologies are considered.

- **Results** Advantages and disadvantages of each mission are presented. Improvements to the custom flyby algorithm are also discussed.

## 1.3 Social and economic impact

Public scrutiny often targets science funding, demanding evidence of its tangible social and economic benefits. This challenge is particularly pronounced in fields like astronomy and astrodynamics, where justifying investments for exploring distant celestial objects and phenomena is difficult.

A pivotal outcome of the research process lies in the array of technologies conceived, subsequently finding diverse applications for societal improvement. Consider the iconic Apollo program as an example. The groundbreaking technologies developed for the success of Apollo missions, including the formidable Saturn V rocket, the versatile Lunar Module, and the pioneering Apollo Guidance Computer (AGC) depicted in Figure 1.1, have transcended their original purposes and found invaluable utility across various fields.

**Fig. 1.1:** The figure displays two key components of the AGC: the Computer Unit, constructed entirely from NOR gate integrated circuits on the left, and the Display and Keyboard (DSKY) on the right, used by astronauts to interact with the AGC.

These technologies incorporated novel approaches, notably the utilization of integrated circuits (ICs). The challenges addressed during this era have paved the way for modern advancements, evident in the widespread adoption of fly-by-wire technology in commercial airplanes and the ubiquitous presence of ICs in various devices.

Similarly, the study of interstellar objects holds promise for fostering innovation in propulsion, navigation, guidance, and observation technologies. These advancements can be subsequently adapted and applied in other disciplines, such as Earth observation, satellite communications, and space debris mitigation.

## 1.4 Software used in this project

Modern astrodynamics and orbital mechanics require the use of numerical routines and software. In this project, the following software were used: poliastro and Ansys Systems Tool Kit (STK). All code is hosted in the https://github.com/jorgepiloto/tfm repository.

The Python library named poliastro focuses on astrodynamics and orbital mechanics. It provides tools focused on the analysis and design of orbits. Despite poliastro being archived, the author is a former maintainer of the project. This allowed the author to build a set of custom numerical routines and improvements on top of the original source code. Main capabilities from poliastro include orbit visualization, ephemerides manipulation, and porkchop plots among many others. For these last figures, their original source code was parallelized to maximize the performance, reducing computation times.

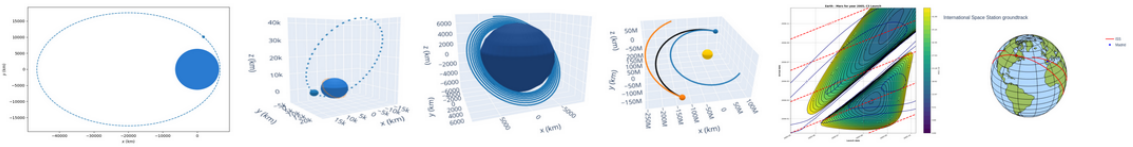

**Fig. 1.2:** A collection of use cases of poliastro. Examples include orbit plotting in 2D and 3D, perturbations, and porkchop plots.

STK, on the other hand, is a commercial software that provides a set of tools that extend beyong astrodynamic calculations. It is used for mission analysis, allowing customers to design, analyze, and visualize complex systems. Its outstanding performance, accuracy, visualization, and animation capabilities make this tool a standard in the aerospace industry. Main capabilities used from STK include validation of results and animations. Regarding animations, these are presented in the slides acompanying the defense of this project.

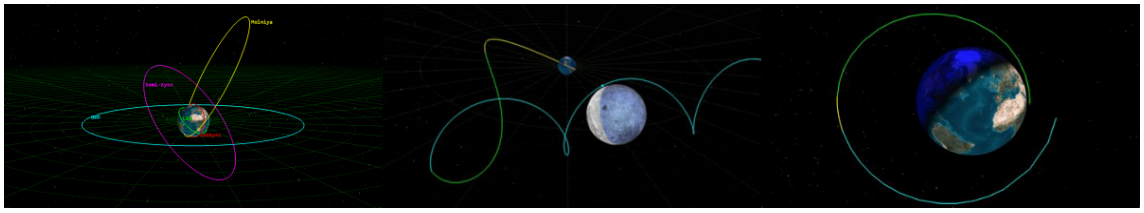

**Fig. 1.3:** A collection of use cases of STK. Examples include orbit plotting in 3D, cislunar trajectories, and orbit transfer optimization.

# 2 Review of interstellar interlopers

In this chapter, a complete review of the state of the art of the field of interstellar interlopers is presented. This includes the definition of interstellar objects, their naming convention, their main attributes, the history of the discovery of these objects, and the role of the solar apex.

## 2.1 Fundamentals

This section provides a brief overview of interstellar objects. For a deeper review on interstellar objects, the reader is referred to Jewitt and Seligman 2023, whose contribution to the topic is invaluable.

### 2.1.1 Definition

Interstellar objects (ISOs) are asteroids, comets or planetary bodies moving through interstellar medium (ISM) without being gravitationally bound to a star. Eventually, ISOs can pass through a planetary system, such as the solar system. Some of them may be even captured, as suggested by Napier et al. 2021.

ISOs are also referred to as interstellar interlopers Jewitt and Seligman 2023, as they can be seen as intruders travelling through a different system from their original one.

### 2.1.2 Origin

There are different mechanisms that can lead to the ejection of ISOs from their original system. The most common are:

- **Stellar encounters.** ISOs can be ejected from their original system due to gravitational interactions with other stars. This mechanism is particularly relevant in dense stellar environments, such as globular clusters, see Fouchard et al. 2011.

- **Planetary encounters.** Planetary encounters can also lead to the ejection of ISOs. This mechanism is particularly relevant in planetary systems with large planets, such as Jupiter and Saturn, see Horner et al. 2003.

- **Stellar explosions.** Supernovae and other stellar explosions can also lead to the ejection of ISOs. These events can provide the necessary energy to eject ISOs from their original system, see Portegies Zwart et al. 2018.

### 2.1.3 Abundance

The abundance of ISOs in the galaxy is still an open question due to the lack of enough data to make a reliable estimation. This lack of data has lead researchers to generate synthetic populations of ISOs to estimate density limits. Table 2.1 shows the density limits estimated by different studies:

| Study | Density limit ($1/pc^3$) | Density limit ($1/AU^3$) |
|---|---|---|
| Gaidos et al. 2017 | $1.0 \times 10^{14}$ | $1.1 \times 10^{-02}$ |
| Jewitt, Luu, et al. 2017 | $8.0 \times 10^{14}$ | $9.1 \times 10^{-02}$ |
| Portegies Zwart et al. 2018 | $1.0 \times 10^{14}$ | $1.1 \times 10^{-02}$ |
| Feng and H. R. A. Jones 2018 | $4.8 \times 10^{13}$ | $5.5 \times 10^{-03}$ |
| Fraser et al. 2018 | $8.0 \times 10^{14}$ | $9.1 \times 10^{-02}$ |
| Do et al. 2018 | $2.0 \times 10^{15}$ | $2.3 \times 10^{-01}$ |

Table 2.1: Density limits estimated by different studies. Note that future discoveries and improvements in detection techniques can lead to different estimations. Adapted from the original review of Moro-Martín 2023.

### 2.1.4 Expected orbit attributes

Discretizing whether a body is an ISO is a challenging task. This is particularly true for small objects, which are harder to detect and track, leading to larger measurement errors when defining their orbits.

The following attributes can indicate the interstellar nature of an object:

- **Hyperbolic orbit.** ISOs must present hyperbolic orbits since they are not gravitationally bound to the Sun. This translates into eccentricities greater than the unity. Hyperbolic eccentricities have been identified in our solar system but attributed to the gravitational pull of the outter planets.

- **High relative velocity.** Interstellar interlopers present high relative velocities with the planets and other bodies of the system they are passing through. This is a consequence of their interstellar origin.

- **High inclination with respect to invariable plane of the solar system.** Although ISOs are expected to be discovered with any inclination, a high inclination with respect to the invariable plane of the solar system can be an indication of their interstellar origin. Since an ISO is not gravitationally bound to the Sun, it is unlikely that its angular momentum is aligned with the one of the solar system.

### 2.1.5 Interstellar impostors

Note that the attributes presented in subsection 2.1.4 are not exclusive to ISOs. For example, a body with a high inclination and a hyperbolic orbit could be a comet from the Oort cloud[1] affected by the gravitational pull of the outter planets.

These objects are known as *interstellar impostors*, as they exhibit their properties but not their origin. Other authors like Higuchi and Kokubo 2019 refer to these objects as hyperbolic Oort cloud comets (HOCs). HOCs are more likely to be ejected into the ISM rather than falling into the internals of the solar system, see Francis 2005. However, Peña-Asensio, Visuri, et al. 2024 have found an Earth impactor with a hyperbolic orbit, which is believed to be an HOC resulting from the perturbation of Oort's cloud.

## 2.2 Naming

The naming of interstellar objects is imposed by the International Astronomical Union (IAU). The IAU has established a nomenclature for interstellar objects, which must follow the format[2]:

[Prefix]/[Year][Half-month][Number]

**Prefix** is a letter indicating the nature of the object according to table 2.2. Once the interstellar nature has been confirmed, the prefix sticks to I.

| Object | Prefix |
|---|---|
| Comet | C |
| Periodic comet | P |
| Unknown orbit comet | X |
| Dissapeared comet | D |
| Interstellar object | I |

Table 2.2: IAU prefixes for comets and interstellar objects.

[1] Oort cloud is a trans-Neptunian region that extends from 2000 to 50000 AU. It is the source of long-period comets and believed to contain a total mass of 5 Earth masses made up to $10^{12}$ - $10^{14}$ objects.

[2] Exceptions exist. Identifiers may include the name of the discoverers or even popular names due to legacy reasons.

**Year** matches the number of the year of discovery while **half-month** is a letter indicating the period of the year when the discovery was made according to table 2.3.

| Latin Letter | Half-Month | Latin Letter | Half-Month |
|---|---|---|---|
| A | Jan. 1-15 | B | Jan. 16-31 |
| C | Feb. 1-15 | D | Feb. 16-29 |
| E | Mar. 1-15 | F | Mar. 16-31 |
| G | Apr. 1-15 | H | Apr. 16-30 |
| J | May 1-15 | K | May 16-31 |
| L | June 1-15 | M | June 16-30 |
| N | July 1-15 | O | July 16-31 |
| P | Aug. 1-15 | Q | Aug. 16-31 |
| R | Sep. 1-15 | S | Sep. 16-30 |
| T | Oct. 1-15 | U | Oct. 16-31 |
| V | Nov. 1-15 | W | Nov. 16-30 |
| X | Dec. 1-15 | Y | Dec. 16-31 |

Table 2.3: IAU half-month identifier.

Finally, the **Number** is the digit representing the order of discovery within the half-month of discovery. This number starts at 1 for the first discovered object of the half-month.

## 2.3 Discovered objects

In 2017 the first interstellar object was discovered. Initially designated as 1I/2017 U1, this object is now commonly referred to as 1I/'Oumuamua. Subsequently, in 2019, the discovery of the second interstellar object occurred. Initially thought to be a comet, it was named C/2019 Q4. Upon confirming its interstellar nature, this object became known as 2I/Borisov.

Despite originating from the same interstellar realm, both objects exhibited distinct properties. These unique characteristics are thoroughly examined and discussed in the subsequent subsections. For a more comprehensive analysis of these objects and their attributes, reader is encouraged to refer to the work by Jewitt and Seligman 2023.

### 2.3.1 1I/'Oumuamua

'Oumuamua was initially spotted on October 19, 2017, by the Pan-STARRS1 telescope in Hawaii. Initially designated as a comet under the identifier C/2017 U1, it was later reclassified as an asteroid. Figures 2.1, 2.2, and 2.3 show the orbit with respect to the ecliptic of this interloper at the moment of its discovery from different perspectives.

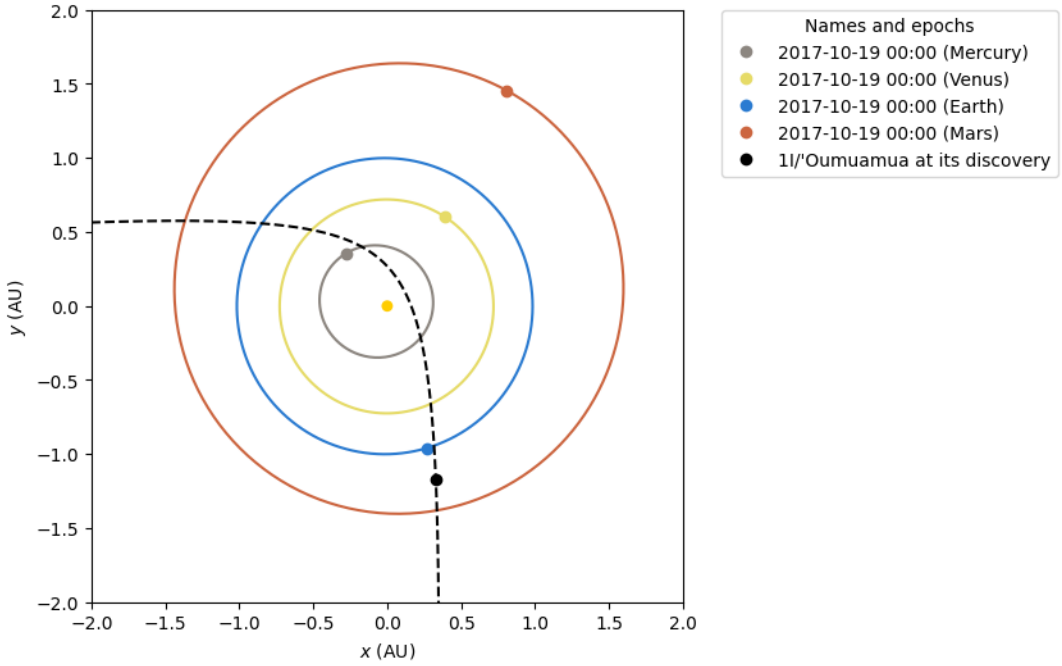


**Fig. 2.1:** Top view of the orbit of 1I/'Oumuamua through the solar system at the time when it was discovered. The interloper presented a perihelion distance of 0.25 AU, closer than Mercury. 1I/'Oumuamua exhibits a retrograde orbit moving towards the bottom of this figure.

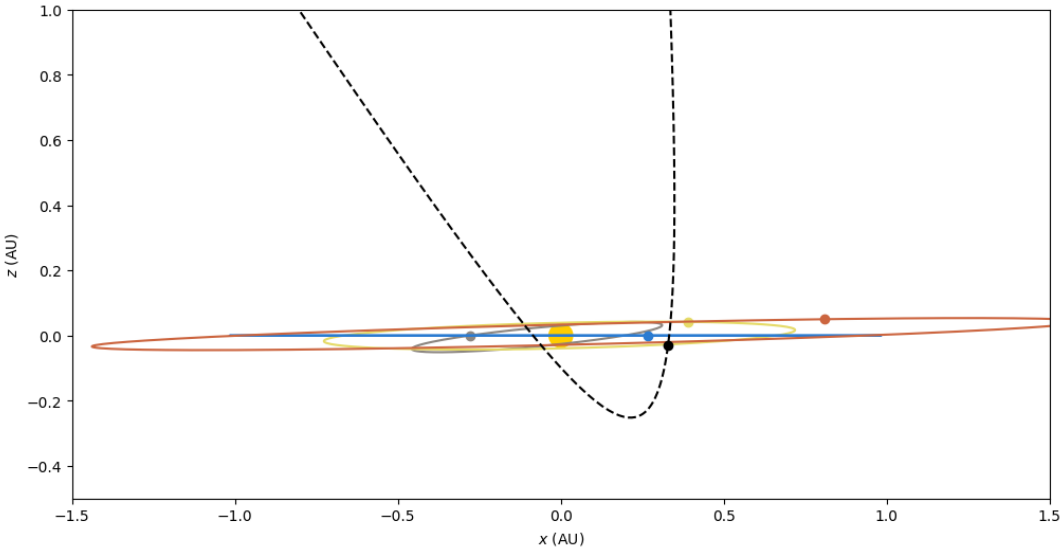


**Fig. 2.2:** Front view of the orbit of 1I/'Oumuamua through the solar system at the time when it was discovered. This perspective allows to visualize the high inclination of 1I/'Oumuamua as it passes through the solar system. Legend shared with figure 2.1.

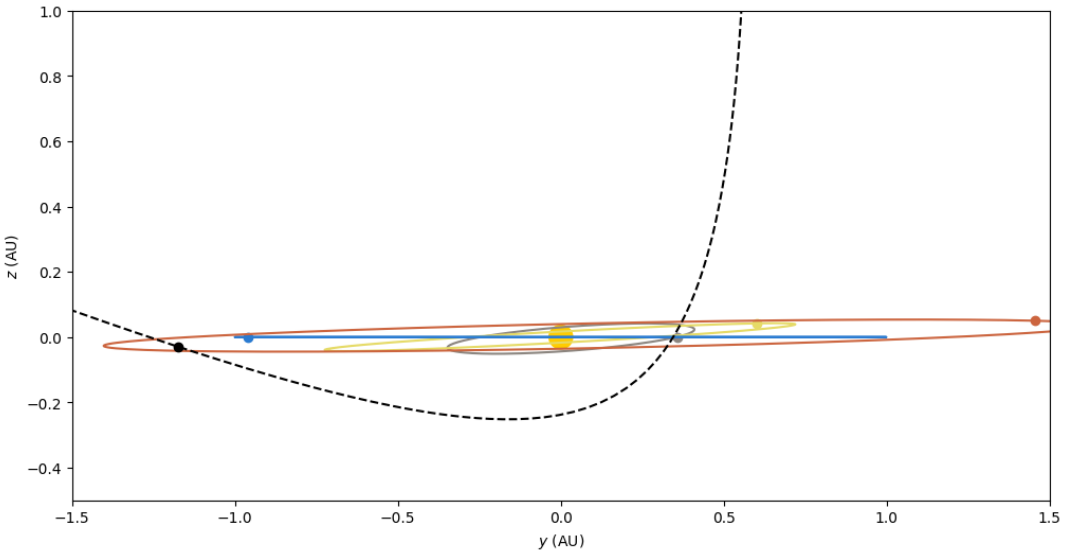


**Fig. 2.3:** Side view of the orbit of 1I/'Oumuamua through the solar system at the time when it was discovered. This perspective allows to visualize the retrograde motion of 1I/'Oumuamua as it passes through the solar system. Legend shared with figure 2.1.

'Oumuamua's orbit was calculated to be highly eccentric, with an eccentricity of 1.20, indicating a hyperbolic trajectory. Its velocity was estimated to be approximately 26.0 km/s. Upon entering the solar system, it approached from the direction $\alpha_{\mathrm{ICRS}}$, $\delta_{\mathrm{ICRS}} = 279°.804$, $+33°.997$, displaying an inclination significantly deviating from the solar system's invariant plane and closely aligning with the solar apex, as discussed in Mamajek 2017. These characteristics collectively suggest an interstellar origin, as elucidated in subsection 2.1.4. Table 2.4 provides a summary of 1I/'Oumuamua's orbit elements as of November 23, 2017.

| Element | Value |
|---|---|
| Eccentricity ($e$) | 1.20 |
| Semi-major axis ($a$) | -1.27 AU |
| Perihelion ($q$) | 0.26 AU |
| Inclination ($i$) | 122.74 deg |
| Longitude of the ascending node ($\Omega$) | 24.59 deg |
| Argument of perihelion ($\omega$) | 241.81 deg |
| Mean anomaly ($M$) | 51.16 deg |
| Mean motion ($n$) | 0.69 deg/d |
| Time of perihelion passage ($T_p$) | 2017-Sep-09.50732138 |

Table 2.4: Orbit elements of 1I/'Oumuamua as provided by the NASA SBDB.

Surprisingly, this first discovered ISO presented a non-gravitational acceleration that could not be attributed to cometary properties. In addition, observations could not determine jetting of particles, an effect experienced by cometary objects.

'Oumuamua's shape was also a matter of debate. Due to its size, the interloper appeared as a single point in all telescope images, like the one reproduced in figure 2.4. At first, it was estimated to have a cigar-like body. However, later studies solved the best fititng shape that matched the observed lightcurves. The results indicate that 1I/'Oumuamua should have a planar disk shape, see Mashchenko 2019.

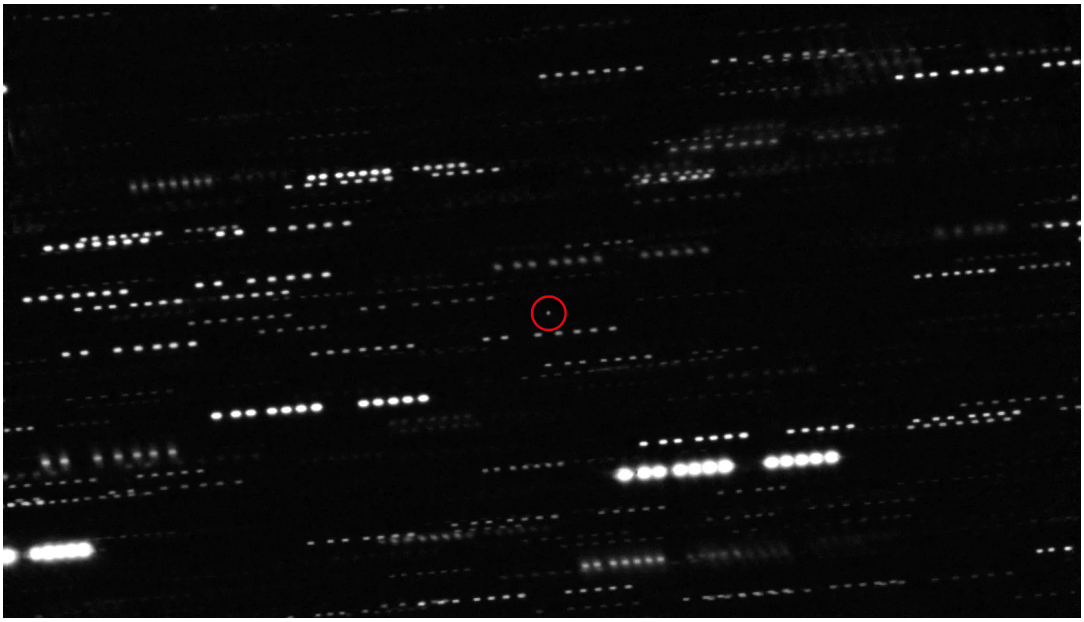

**Fig. 2.4:** 1I/'Oumuamua as seen by the ESO's Very Large Telescope and the Gemini South Telescope. This image was released on September 9, 2023. It shows a combination of images taken by the two telecopes. The object is seen as a point in the center of the image. Background stars are seen as streaks due to the telescope's tracking of the object. No cometary tail or mass ejection is observed, raising questions about the non-gravitational acceleration presented by the interloper.

Unfortunately, 1I/'Oumuamua was discovered after its pasage through the perihelion and could only be observed for about four weeks before becoming to faint. This limited the amount of data that could be gathered about the object, increasing the mistery about the first interstellar object.

### 2.3.2 2I/Borisov

Borisov was first sighted on August 30, 2019, by Gennady Borisov[3]. Initially labeled as a comet bearing the identifier C/2019 Q4, it underwent reclassification as an interstellar object subsequent to the determination of its remarkably high eccentricity. Figure 2.5 shows the orbit of this interloper at the moment of its discovery.

[3]Borisov, an amateur astronomer from Crimea, detected the second interloper using his home-built 0.65 meters telescope.

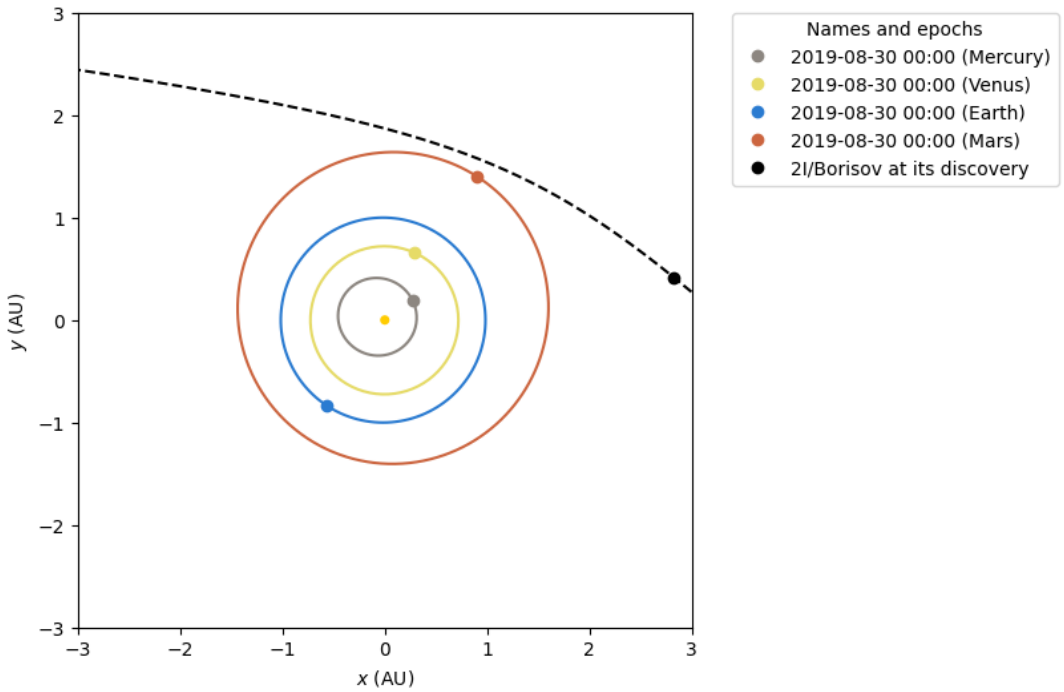


**Fig. 2.5:** Top view of the orbit of 2I/Borisov through the solar system. Its eccentricity is close to 3.36, making it the most eccentric object observed up to date and discarding the possibility of being gravitationally bounded to the Sun. 2I/Borisov presented a perihelion distance of 2.01 AU, closer than Mars.

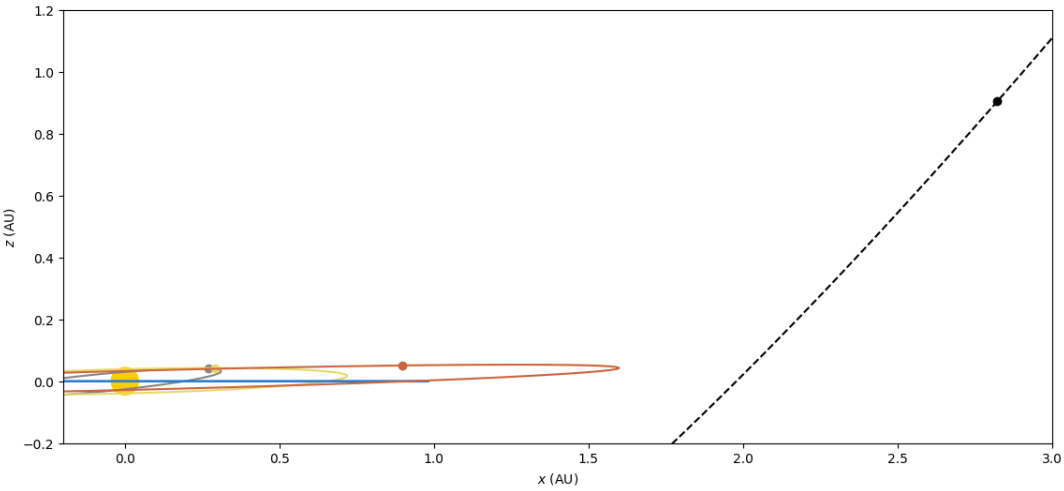


**Fig. 2.6:** Front view of the orbit of 2I/Borisov through the solar system. Despite the apparent close distance with the Martian planet, this view shows that both celestial objects were actually far from each other. Legend shared with figure 2.5.

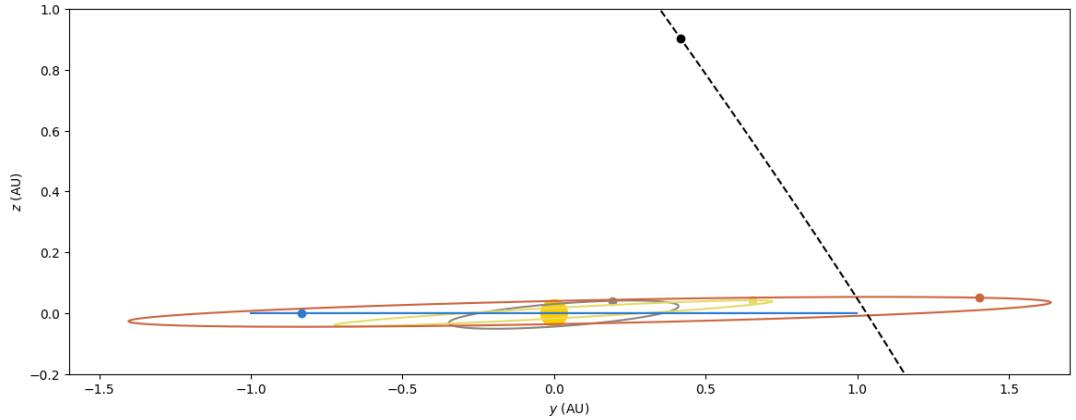


**Fig. 2.7:** Side view of the orbit of 2I/Borisov through the solar system. Even if this view suggests that 2I/Borisov could have a high inclination, the value for this parameter was not as high as the one for the first discovered interloper. Legend shared with figure 2.5.

With an eccentricity of 3.36 and a velocity of 32.2 km/s, 2I/Borisov exhibited a hyperbolic orbit. Its inclination of 44.1 degrees incoming from constellation Cassiopeia further confirmed its ISO nature. Table 2.5 provides a summary of 2I/Borisov's orbit elements as of August 1, 2020.

| Element | Value |
|---|---|
| Epoch ($t$) | August 1, 2020 |
| Eccentricity ($e$) | 3.36 |
| Semi-major axis ($a$) | -0.85 au |
| Perihelion ($q$) | 2.01 au |
| Inclination ($i$) | 44.05 deg |
| Longitude of the ascending node ($\Omega$) | 308.15 deg |
| Argument of perihelion ($\omega$) | 209.12 deg |
| Mean anomaly ($M$) | 296.54 deg |
| Mean motion ($n$) | 1.25 deg/d |
| Time of perihelion passage ($T_p$) | 2019-Dec-08.54507021 |

Table 2.5: Orbit elements of 2I/Borisov as provided by the NASA SBDB.

Unlike 1I/'Oumuamua, 2I/Borisov displayed a cometary tail. Remarkably, the NASA/ESA Hubble Space Telescope captured images of this interloper, as depicted in figure 2.8.

Analysis revealed that the coma of 2I/Borisov contained significantly more carbon monoxide (CO) gas than water ($H_2O$), with abundances exceeding 173%, surpassing typical cometary compositions within our solar system by over threefold. Additionally, hydrogen cyanide (HCN) was also detected in the gas expelled by the comet, with levels comparable to those observed in other solar system comets, see Bodewits et al. 2020.

**Fig. 2.8:** 2I/Borisov as seen by the NASA/ESA Hubble Space Telescope. This image was released on December 12, 2019, when the interloper was close to the Sun. Its cometary properties are evident in this image. 2I/Borisov's tail is seen as a faint streak extending from the object. It is believed that the tail is composed of

### 2.3.3 Other interstellar candidates

The interest in interstellar objects has lead a research on previously discovered objects, in particular interstellar meteors (IM). Interstellar meteors are meter-scale objects that collide with Earth from a trajectory that is gravitationally unbound to the Sun, meaning they originate from outside our solar system.

Two confirmed interstellar meteors have been identified so far:

- CNEOS 2014-01-08 (also known as IM1 or the Manus Island fireball), which was detected in 2014 and confirmed as interstellar in 2022 by the U.S. Space Command, see Siraj and Loeb 2022.
- CNEOS 2017-03-09 (also known as IM2), which was discovered in 2022 and is estimated to have been 10 times more massive than IM1, around 1 meter in size, see Peña-Asensio, Trigo-Rodríguez, et al. 2022.

Both IM1 and IM2 were moving at extremely high speeds relative to the local standard of rest - IM1 at 60 km/s and IM2 at 40 km/s. This high velocity is a key indicator of their interstellar origin. Analysis of the meteors' material strength suggests they were tougher than typical iron meteorites, implying they may not have originated from a planetary system like our own.

## 2.4 The role of the solar apex

Interstellar objects can be discovered from various directions in space. However, it is more common for them to be detected near the direction of the solar apex, as observed with 1I/'Oumuamua (in the constellation Lyra) and 2I/Borisov (in the constellation Cassiopeia).

The solar apex, also known as the apex of the Sun's motion, indicates the direction in which the Sun is traveling relative to the local standard of rest (LSR). Positioned in the constellation Hercules, southwest of the bright star Vega, its visual coordinates are right ascension 18h 28m 0s and declination +30° N. The solar apex moves at a velocity of approximately 19.4 km/s (4.09 AU/year) relative to the local standard of rest, see Dehnen and Binney 1998. Conversely, the solar antapex, situated near the star Zeta Canis Majoris in the constellation Columba, points in the opposite direction. Due to this high relative speed, encounters with intersellar objects are more likely to occur in the direction of the solar apex and present hyperbolic orbits.

Figure 2.9 illustrates the locations of the solar apex and antapex. The radial velocities of nearby stars are denoted by $V_r$, while their proper motions are represented by $\mu$.

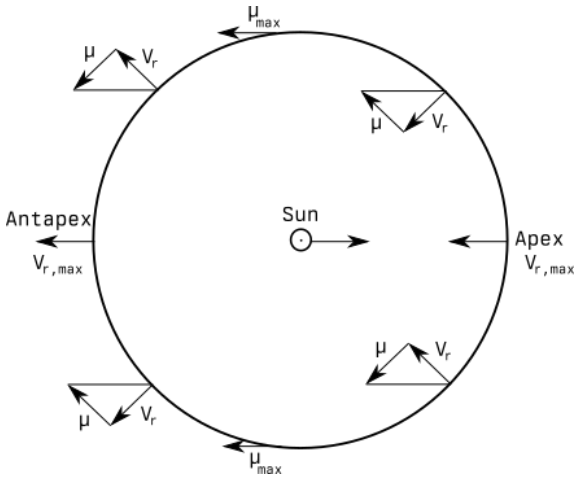


**Fig. 2.9:** The motion of the Sun in the LST. The apex and antiapex are represented in the same and opposite direction of the Sun's motion. The combination of radial veolcities and proper motions of stars in the leads to the apparent motion of stars in the LST moving from the apex towards the antiapex.

As the Sun progresses towards the solar apex, nearby stars appear to diverge from this point in the celestial sphere. Conversely, stars seem to converge towards each other in the direction of the solar antapex.

It is important to note that the Sun's motion within the Milky Way galaxy is not solely restricted to the galactic plane; it also entails an oscillatory movement relative to the plane

spanning millions of years.

Authors like Marčeta 2023 consider the role of the solar apex when generating a synthetic population of interstellar objects in the solar system. Figure 2.10 shows the expected distribution of interstellar interlopers.

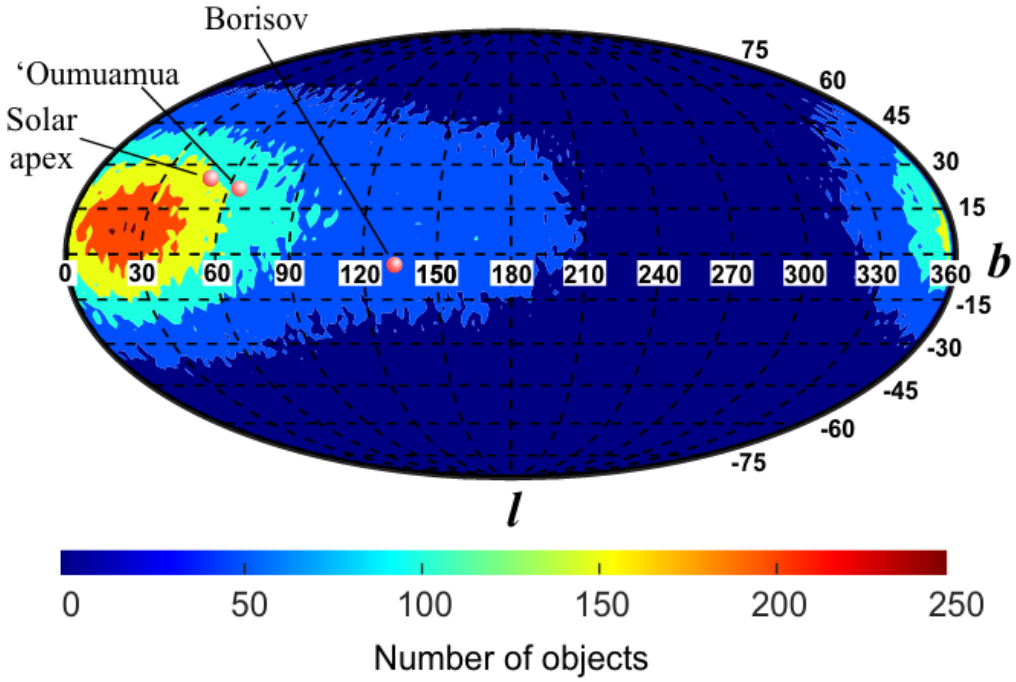


**Fig. 2.10:** The expected distribution of interstellar interlopers in the solar system, represented in a galactic coordinates. A higher density of interstellar interlopers is expected in the direction of the solar apex. The direction of 1I/'Oumuamua and 2I/Borisov is found to be close to this point, located near constellation Lyra. This contour plot is figure 11 of Marčeta 2023 article. It is reproduced under permission of its original author.

Despite this preferred direction, it is important to remember that there is nothing that prevents and ISO to be discovered in other direction. In fact, probabilities for intetifying an interloper approaching in the direction of the solar-antapex are lower, but not null.

# 3 Revisiting targeting missions

In this section, a review on targeting for space missions is presented. The Lambert's problem is revisited together with its big role in targeting. Next, the mathematical model used for this work is exposed. Finally, various mission constrains are collected to showcase the challenged when planning a mission.

## 3.1 Lambert's problem

Lambert's problem is the boundary value problem (BVP) in the context of the restricted two-body problem dynamics. Equation 3.1 models this problem and figure 3.1 depicts its geometry.

$$\ddot{\vec{r}} = -\frac{\mu}{r^3}\vec{r} \quad \begin{cases} \vec{r}(t_1) = \vec{r}_1 \\ \vec{r}(t_2) = \vec{r}_2 \\ \Delta t = t_2 - t_1 \end{cases} \tag{3.1}$$

If the initial position vector $\vec{r}_1$ is the launch position at time $t_1$ and vector $\vec{r}_2$ is the arrival position at time $t_2$, then it is possible to find the targeting orbit required to transfer a spacecraft between the two.

Consider the case where the spacecraft is launched from a planetary body, like the Earth, and is intended to reach an interloper. The ephemeris (position over time) of the central body and the interloper are known. These can be used as the input parameters for solving Lamber's problem for a given time of flight.

The solution to the Lambert's problem returns the values of $\vec{v_1}$ and $\vec{v_2}$. Since the positions vectors are known, the computed velocity vectors complete the state vectors at launch and arrival.

Once the velocity vectors are obtained, their modulus can be used to compute for the required $\Delta v$. This is the increment in the velocity that needs to be achieved by the propulsion system in order to insert the spacecraft into the desired targeting orbit.

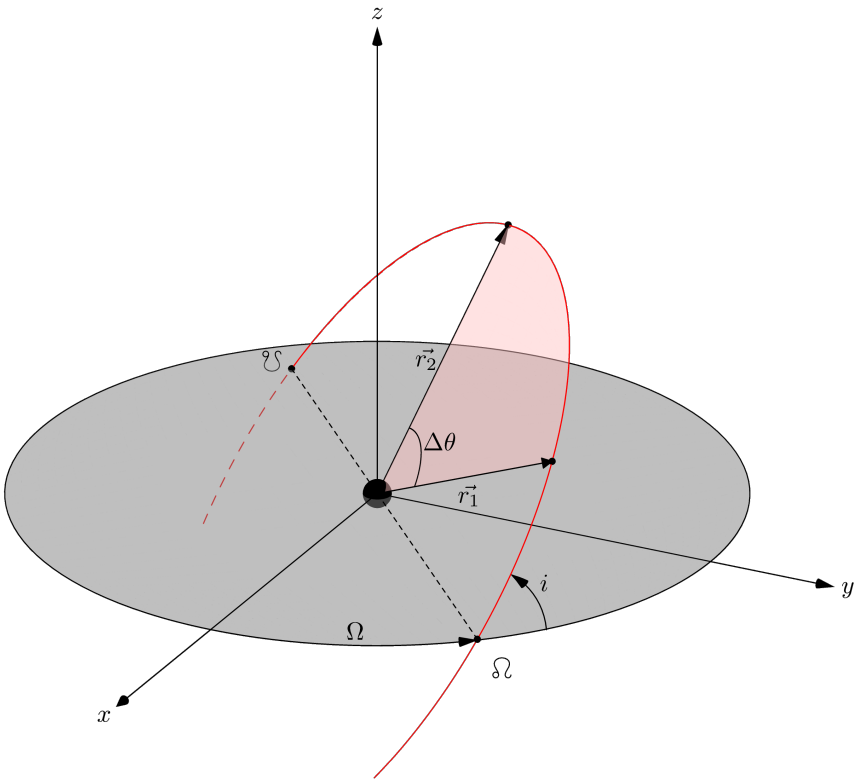


**Fig. 3.1:** Lambert's problem geometry. The targeting orbit is represented by the red curve.

### 3.1.1 Mathematical model

Solving Lambert's problem requires numerical routines. Lots of algorithms have been devised over the last century. The author of this document some of the most popular ones and compared them in performance, see Martinez and Sanjurjo 2021. Any algorithm for solving Lambert's problem operates with the parameters presented in table 3.1.

| Parameter | Description |
|---|---|
| $\mu$ | Gravitational parameter |
| $\vec{r}_1$ | Initial position vector |
| $\vec{r}_2$ | Final position vector |
| $\Delta t$ | Time of flight |
| $M$ | Number of desired revolutions |
| Prograde | Inclination of the final orbit |
| Low path | Type of path when more than two solutions are available |
| Maxiter | Maximum number of iterations when finding a solution |
| Atol | Absolute tolerance of the numerical routine |
| Rtol | Relative tolerance of the numerical routien |

Table 3.1: Parameters accepted by any Lambert's problem solver

This work assumes Lambert's problem in the context of the restricted two-body problem. This means that the only body exherting a gravitational influence is the Sun. Thus, planetary bodies and interstellar interlopers are modeled as points with zero mass and volume. Their gravitational influence is considered negligible except for the escape velocity. Thus, the only body exherting a gravitational force through the propagation of the spacecraft is the Sun. The required $\Delta v$ is modeled as an impulse. This means that the change in the velocity is instantaneous. Perturbations are not considered neither.

By sacrifying the accuracy of the model, the computational complexity of the problem gets reduced. This lowers the time required to solve the problem. Results obtained can be used as a first approximation for further refinement.

## 3.2 Mission constraints

Despite simplifications, the mission design process is still a complex problem. There exists a wide range of mission constraints that can be imposed on the analysis to refine the results and make them more realistic. These include fuel mass, characteristic energy, excess velocity at arrival, time of flight, tracking constraints, and communication constraints. For a complete overview of mission contraints, the reader is referred to Wertz et al. 2011.

### 3.2.1 Fuel mass

The fuel mass is a critical constraint in mission design. For every impulse performed by the spacecraft, a certain amount of fuel is consumed. This loss in mass is modeled according to the Tsiolkovsky rocket equation 3.2:

$$\Delta v = v_e \ln\left(\frac{m_0}{m_f}\right) = I_{sp} g_0 \ln\left(\frac{m_0}{m_f}\right) \tag{3.2}$$

Where $\Delta v$ is the change in velocity, $v_e$ is the exhaust velocity, $m_0$ is the initial mass of the spacecraft, $m_f$ is the final mass of the spacecraft. Other variants of the expression include the $I_{sp}$, the specific impulse of the propulsion system, and $g_0$, the standard gravity.

### 3.2.2 Characteristic energy

The characteristic energy $C_3$ is also a good estimator for the propulsion requirements of a mission.

The $\Delta v$ relates with the characteristic energy $C_3$, also known as specific energy. Equation 3.3 summarizes this relation for hyperbolic orbits:

$$C_3 = v_\infty^2 \tag{3.3}$$

Given a propulsion system, a maximum specific energy is imposed, limiting the maximum $\Delta v$ that the spacecraft can achieve. If a spacraft can not reach a certain characteristic energy, then the mission is not feasible and the target orbit can not be achieved.

The specific energy at launch is related with the payload via 3.2. Figure 3.2 shows the maximum payload for a given characteristic energy for various modern launchers.

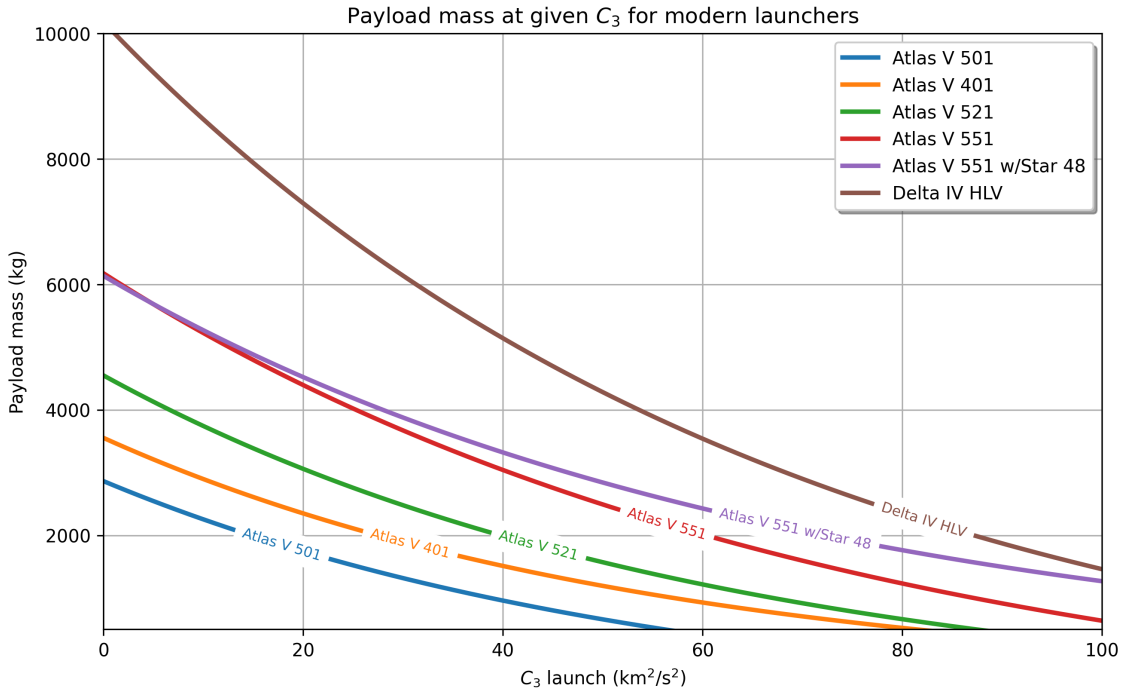


**Fig. 3.2:** Maximum payload for a given characteristic energy for various modern launchers.

### 3.2.3 Excess velocity at arrival

Another mission constraint within the context of interstellar interlopers rendezvous is the excess velocity at arrival. Lauch and arrival velocities are used to compute the impulsed required to reach the target orbit. The first impulse $\Delta v_1$ is used to launch the spacecraft into the target orbit. The second impulse $\Delta v_2$ is used to adapt to the orbit of the interloper, leading to a rendezvous. Thus, two scenarios are possible:

- **Targeting of the interloper.** The spacecraft overshoots the target by not applying the final impulse. This ahieves a greater launch impulse as more fuel mass can be

allocated for this task. However, the spacecraft is not able to rendezvous with the interloper, as the second impulse is never applied.

- **Rendezvous with the interloper.** The spacecraft performs the arrival impulse to adapt to the orbit of the interloper. This reduces the amount of fuel available for the launch impulse but allows the spacecraft to follow the interloper.

Wether the spacecraft overshoots the target or rendezvous with the interloper, the excess velocity at arrival is a critical parameter.

### 3.2.4 Time of flight

The time of flight is another important constraint in mission design. It refers to the elapsed time between the launch and the rendezvous with the interloper. Usually, short times of flight are preferred. They reduce the exposure to space radiaiton, which can affect the spacecraft and its electronics. However, short time of flights require greater fuel mass and thus greater propulsion to achieve greater speeds for covering the astronomical distances between the launch and arrival positions.

### 3.2.5 Tracking constraints

The spacecraft must be able to track the interloper and its own position relative to the stars background. By doing so, the spacecraft can assert if it is on the right orbit and if it is following the interloper correctly.

However, tracking a small object in deep space is a challenging task. For example, 1I/'Oumuamua did not presented any cometary activity, having an absolute magnitude of $M = 22$ (JPL SBDB) which made it difficult to observe and track it. On the other hand, 2I/Borisov exhibited a coma, making it more visible by having a magnitude of $M = 16$, see Jewitt, Hui, et al. 2020. Despite these challenges, the success of missions like DART who used star trackers and in-situ data processing for identifying the target, see Daly et al. 2023, proof that it is possible to track small celestial bodies.

# 4 Direct transfer analysis

This chapter presents the direct transfer analysis performed on the two discovered interstellar objects, 1I/'Oumuamua and 2I/Borisov. The algorithm used is the one devised by Izzo 2014, as it is proven to be more accurate and faster than other classical algorithms, see Martinez and Sanjurjo 2021. The ephemerides for 1I/'Omuaumua and 2I/Borisov are obtained from JPL Horizons API service. These are propagated under the two-body assumption to simplify the analysis. Propagation starts on January 1, 2016 and ends on January 1, 2035.

The analysis includes porkchop plots for quickly visualizing different mission constraints. The optimum transfers are computed and their figures are generated for better undesrtanding the orbit. A short discussion on the obtained values is presented at the end of the chapter.

## 4.1 Characteristic energy at launch

The characteristic energy for launch is the energy required to set a spacecraft into the desired targeting orbit. This analysis assumes that the spacecraft launches from Earth, which is modeled as a point with no mass and arrives at the target interloper, modeled again as a massless point. The only force acting on the spacecraft is the gravitational force of the Sun.

Before launching, the spacecraft has the velocity of Earth, $\vec{v_\oplus}$. At launch, the spacecraft presents an heliocentric velocity $\vec{v_{\infty,1}}$ that matches the solution of Lambert's problem. Vector $\Delta\vec{v}$ is the difference between the two velocities, and its modulus matches the required impulse velocity, as stated in Equation 4.1.

$$\Delta v_1 = \|\vec{v_{\infty,1}} - \vec{v_\oplus}\| \tag{4.1}$$

The value of $\Delta v_1$ can be used in Equation 3.3 for solving the characteristic for launch.

### 4.1.1 1I/'Oumuamua

Porkchop plots for 1I/'Oumuamua representing the characteristic energy for launch are shown in figure 4.1 and figure 4.2.

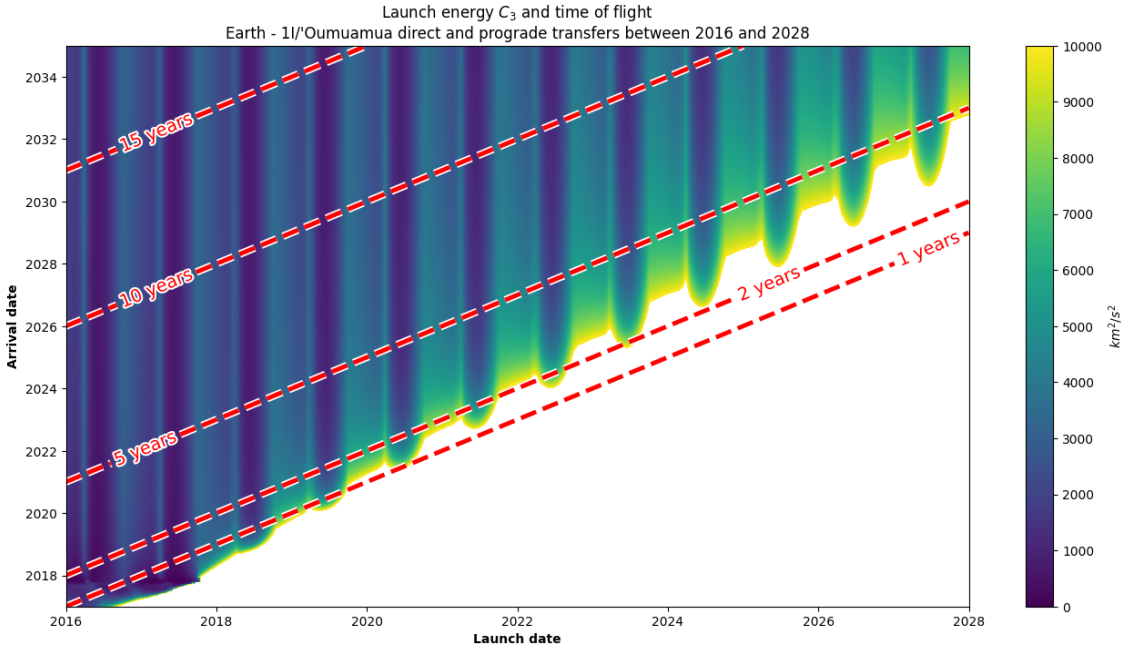


**Fig. 4.1:** Launch energy porkchop plot for 1I/'Oumuamua for a direct and prograde transfer showing the isolines for the time of flight required for a targeting. A region of low transfer energy is located in the lower left corner.

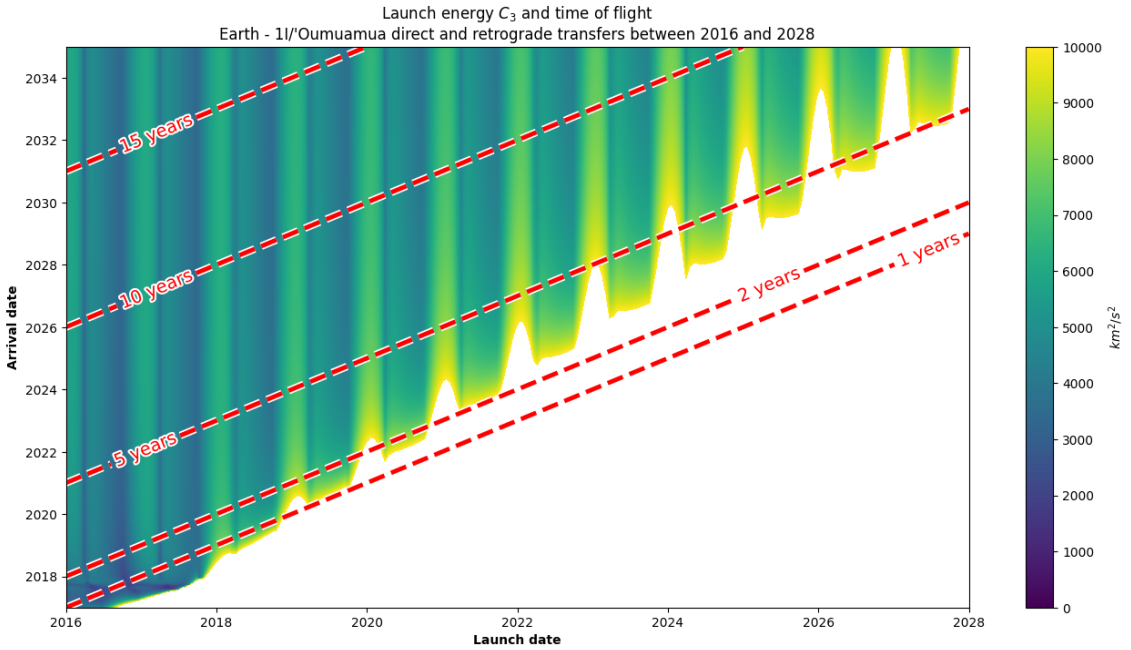


**Fig. 4.2:** Launch energy porkchop plot for 1I/'Oumuamua for a direct and retrograde transfer showing the isolines for the time of flight required for a targeting.

In figures 4.1 and 4.2, shorter time of flights require higher characteristic energies for launch. One may think that a retrograde transfer orbit would be more efficient considering that 1I/'Oumuamua has this kind of inclination. However, retrograde orbits do not benefit from Earth's velocity at launch, which makes them less efficient. Therefore, characteristic energies for retrograde transfers are higher than for prograde transfers.

Both porkchop plots present a pattern whose solutions alternate between low and high characteristic energies. This pattern is a consequence of the relative position of the earth with respect to the target. Low energy solutions correspong to positions in which the velocity of the Earth gets aligned with the launch velocity vector.

Note that, despite some areas in the figures not being colored, they have a solution. These areas do not show any color due to the upper limit for the characteristic energy at launch imposed of $C_3 = 10000$ km$^2$/s$^2$, imposed by the author. This allows for a better representation of the porkchops to visually identify regions. This allows to identify a small region, between years 2016 and 2018 where values for $C_3$ are lower.

### 4.1.2 2I/Borisov

Porkchop plots for 2I/Borisov representing the characteristic energy for launch are shown in figure 4.3 and figure 4.4. These figures remember to the ones for 1I/'Oumuamua, although they present different numerical values. Again, the shorter the time of flight, the greater the characteristic energy for launching the spacecraft. Retrograde transfers, once again, are less efficient than prograde and a pattern of low and high energy solutions is present.

Values for 2I/Borisov's characteristic energy at launch are lower than 1I/'Oumuamua for the same time of flight. Despite having a greater relative velocity, 2I/Borisov has a lower inclination than 1I/'Oumuamua with respect to the ecliptic. Thanks to this low inclination, a spacecraft departing from Earth can benefit a bit more from Earth's velocity at launch time, reducing the required energy.

As a result of previous situation, a set of low energy transfers appears between years 2016 and 2020. However, as opposite to 1I/'Oumuamua, these seem to extend a bit further in the direction of the arrival date. This region is analyzed in detail in the next section.

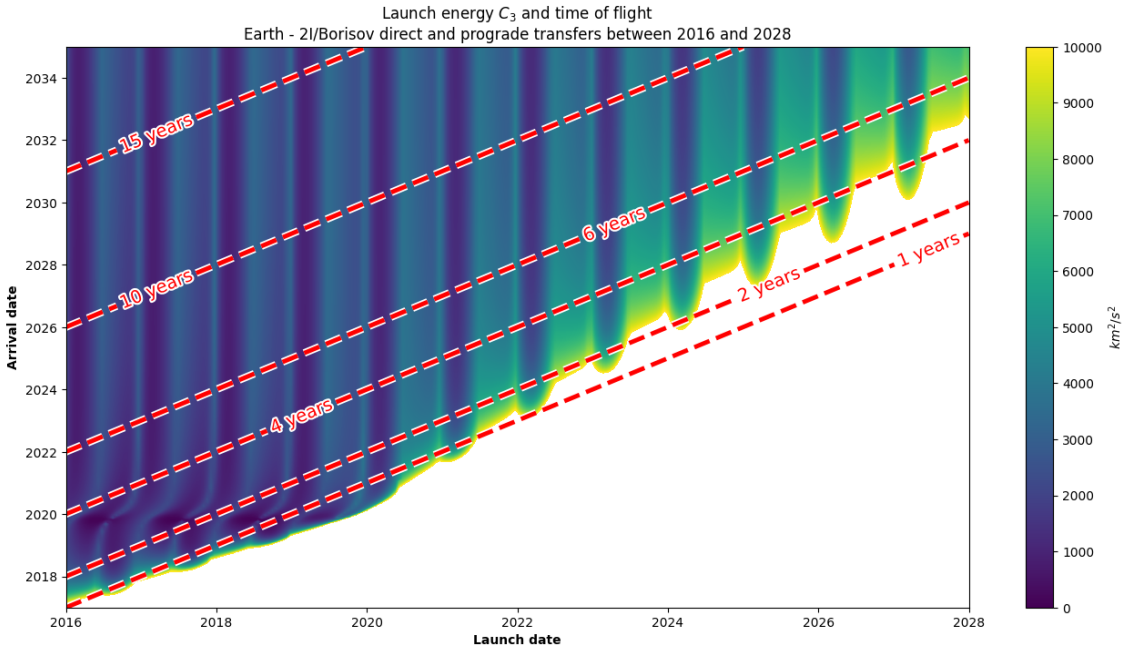


**Fig. 4.3:** Launch energy porkchop plot for 2I/Borisov for a direct and prograde transfer showing the isolines for the time of flight required for a targeting. Values under 1000 $km^2/s^2$ show in the lower left corner. This region should be further explored.

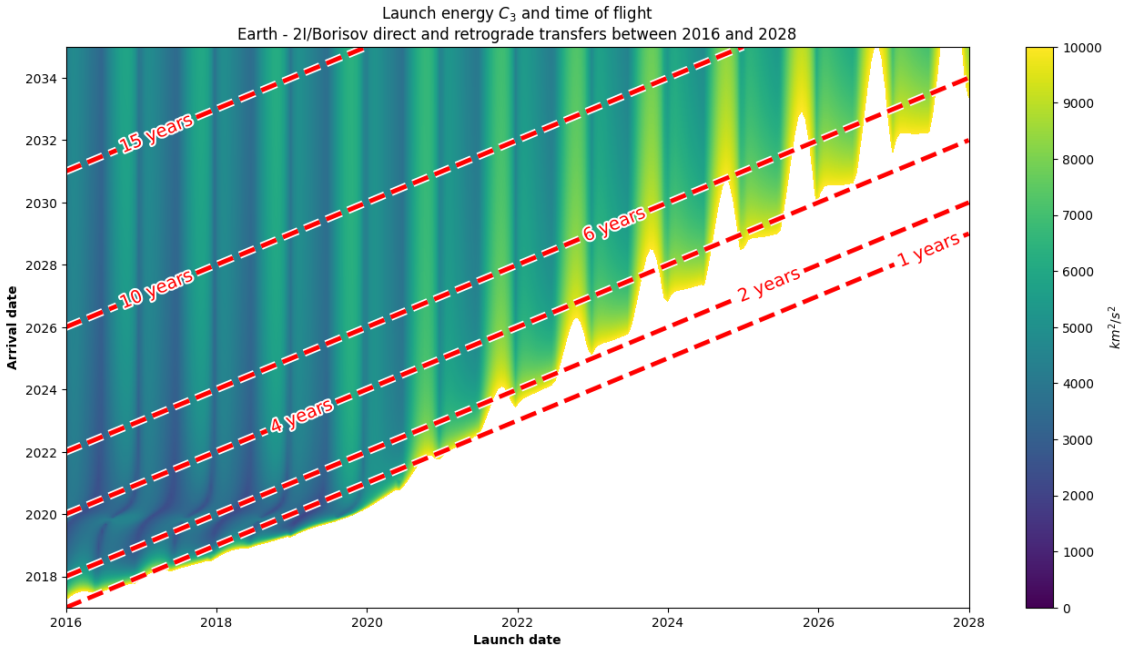


**Fig. 4.4:** Launch energy porkchop plot for 2I/Borisov for a direct and retrograde transfer showing the isolines for the time of flight required for a targeting. The retrograde case shows energies too large for a suitable transfer.

## 4.2 Excess velocity at arrival

The excess velocity at arrival is the difference between the velocity of the spacecraft and the velocity of the interloper at arrival. The velocity of the spacecraft at arrival is denoted by $v_{\infty,2}^{\rightarrow}$. Note that this velocity represents the velocity after the second impulse of Lambert's maneuver, leading to a rendezvous with the interloper. The velocity of the interloper at arrival is $v_{\mathrm{ISO}}^{\rightarrow}$. Thus, the excess velocity at arrival is:

$$\Delta v_2 = \|v_{\infty,2}^{\rightarrow} - v_{\mathrm{ISO}}^{\rightarrow}\| \tag{4.2}$$

As discussed in subsection 3.2.3, applying this last impulse can be avoided on behalf performing a targeting mission. This allows to allocate more $\Delta v$ for the first impulse.

### 4.2.1 1I/'Oumuamua

Porkchop plots for 1I/'Oumuamua representing the excess velocity at arrival are shown in figure 4.5 and figure 4.6.

For short-duration flights, the velocity surplus upon arrival is notably higher, contrasting with longer flights where the surplus is reduced. Both prograde and retrograde transfers exhibit a similar trend in arrival velocity.

Interestingly, the isolines depicting excess arrival velocity reveal a distinctive pattern, all originating from a shared point circa late 2017 for both launch and arrival.

Of particular significance is the area delineated by the 2.0 km/s isoline in prograde transfers, representing an optimal velocity for rendezvous with the interloper given current technological capabilities. Examining the time-of-flight data in Figure 4.1, this region necessitates a minimum trip duration of at least 5 years. It is worth noting that the only constraints on flight duration are those dictated by mission requirements.

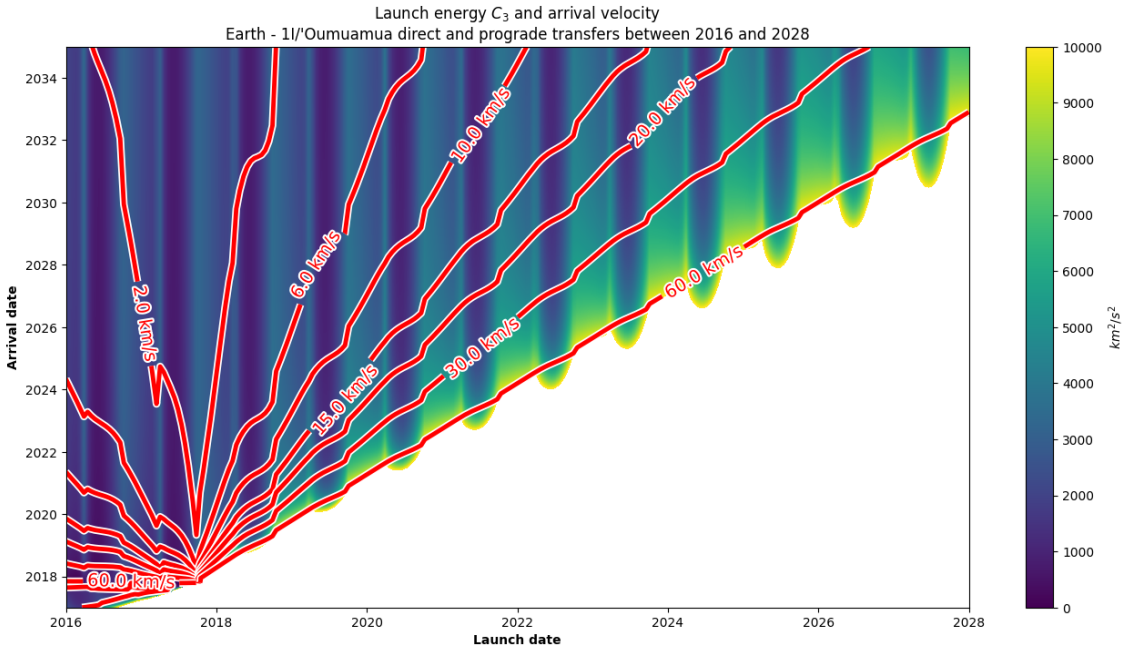


**Fig. 4.5:** Launch energy porkchop plot for 1I/'Oumuamua for a direct and prograde transfer showing the isolines for the arrival velocity required for a rendezvous.

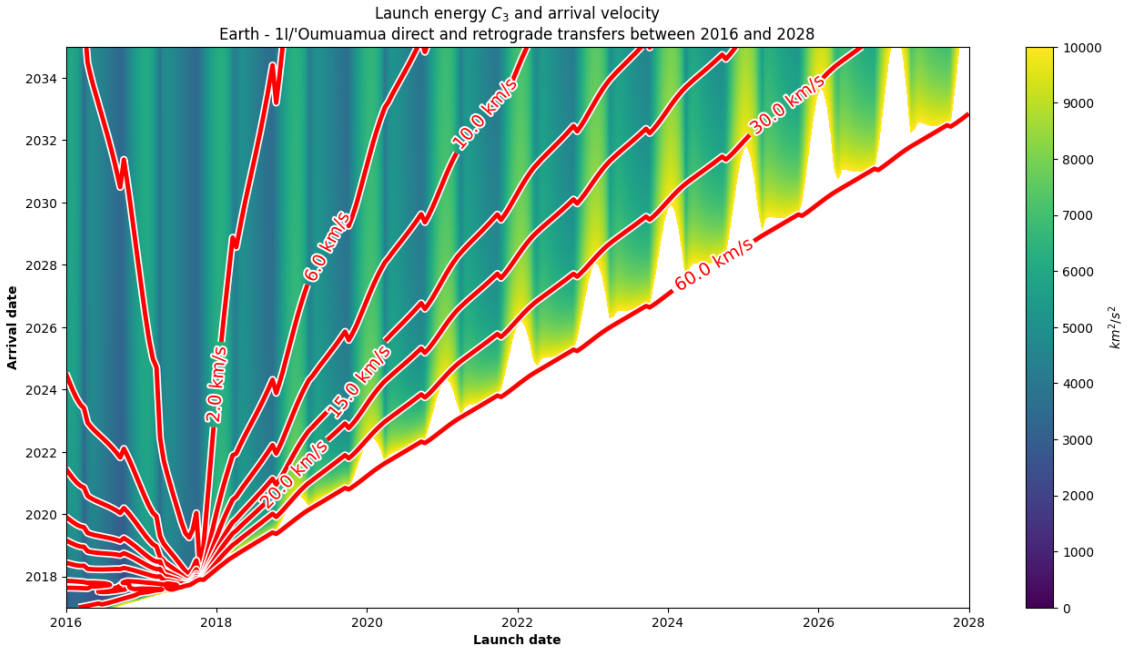


**Fig. 4.6:** Launch energy porkchop plot for 1I/'Oumuamua for a direct and retrograde transfer showing the isolines for the arrival velocity required for a rendezvous.

### 4.2.2 2I/Borisov

Porkchop plots for 2I/Borisov representing the excess velocity at arrival are shown in figures 4.7 and 4.8.

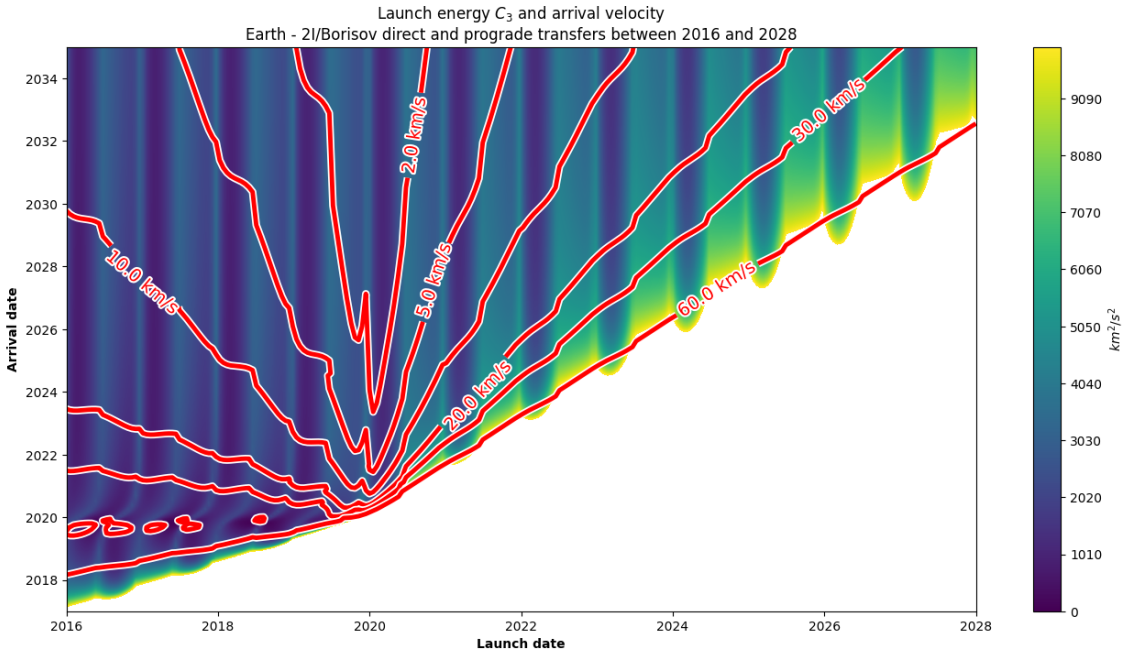


**Fig. 4.7:** Launch energy porkchop plot for 2I/Borisov for a direct and prograde transfer showing the isolines for excess velocity at arrival for a rendezvous.

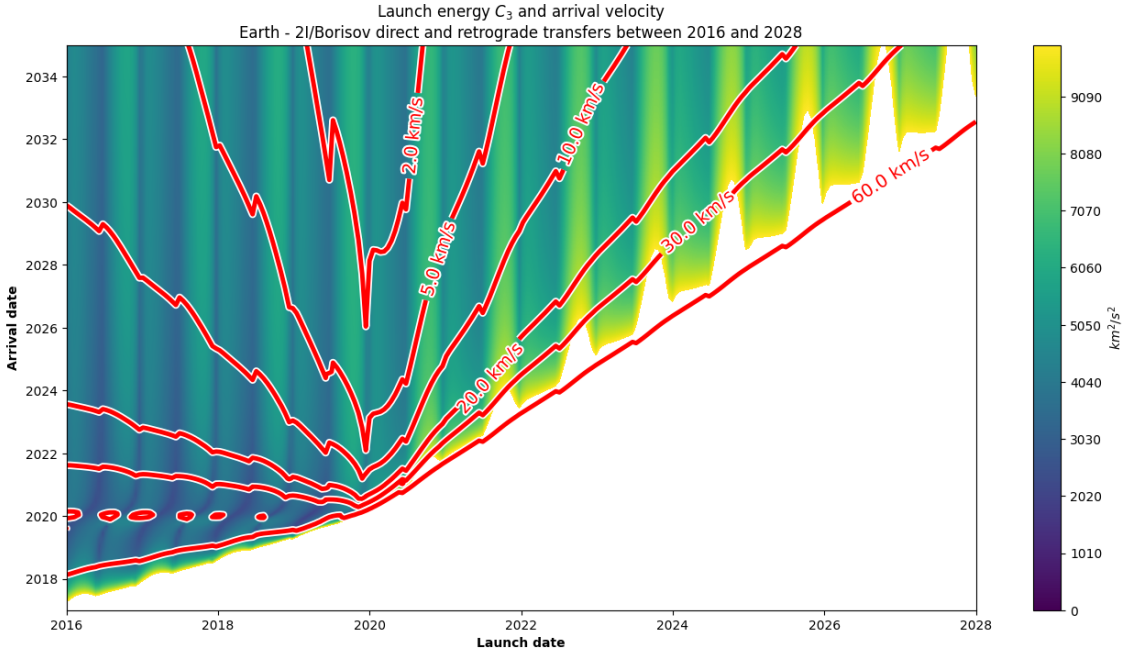


**Fig. 4.8:** Launch energy porkchop plot for 2I/Borisov for a direct and retrograde transfer showing the isolines for excess velocity at arrival for a rendezvous.

Once again, the excess velocity at arrival for 2I/Borisov remembers the ones for the case of 1I/'Oumuamua. Again, the values are different and higher for the second discovered interloper.

Similarly to 1I/'Oumuamua, the lines for the arrival velocity start at a common point. In this case, the point is located at the beginning of 2020 for launch dates. However, the main difference with the first discovered interloper is that a series of closed lines shows for an arrival at year 2020. This could indicate a periodic solution. This region is analyzed in detail in the next section.

## 4.3 Optimum transfer

Once direct transfers (prograde and retrograde) have been computed for each pair of launch and arrival dates, the most optimum transfer orbit can be identified.

It is important to define the concept of optimum transfer. In this context, this term refers to the orbit whose launch energy is the lowest. Other mission constrains may be considered but for the purpose of this work, the launch $C_3$ energy is the only parameter considered. The reason is that the $\Delta v_1$ required for a direct transfer is a limiting factor for nowadays technology.

Porkchps represented in figures 4.1 and 4.3 contain an optimum transfer maneuver. This section analyzes the most optimum transfer for each interloper, including a detailed description of the trajectory and the impulses required.

### 4.3.1 1I/'Oumuamua

Among the prograde and retrogade direct transfers, the most optimum transfer is contained in the set of prograde orbits. Analyzing figure 4.1 in detail, it is possible to limit the value of the characteristic energy at launch to ignore high speed impulse solutions. This reveals figure 4.9. The analysis is also expanded for considering the arrival velocity. This is depicted in figure 4.10.

The values associated with the point with the lowest characteristic energy for launching a spacecraft, indicated with a red cross in the figures, are collected in table 4.1.

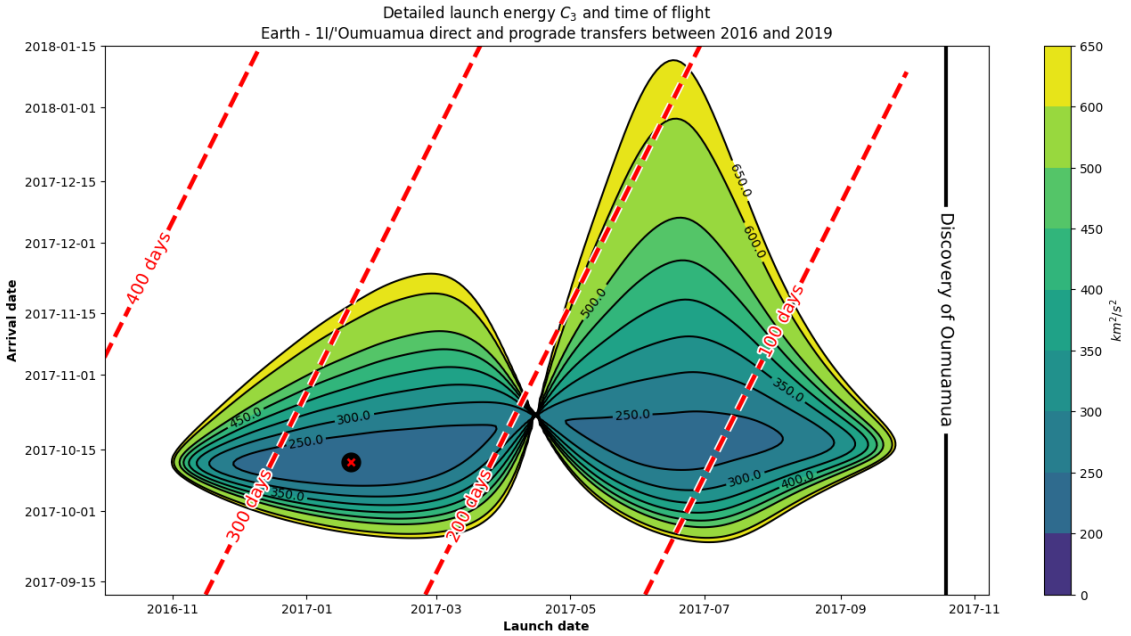


**Fig. 4.9:** Detailed porkchop showing the optimum transfer for 1I/'Oumuamua. The optimum transfer point is represented by a black dot with a red cross. A region close to 200 $km^2/s^2$ is found. Escape velocity from Earth is considered too.

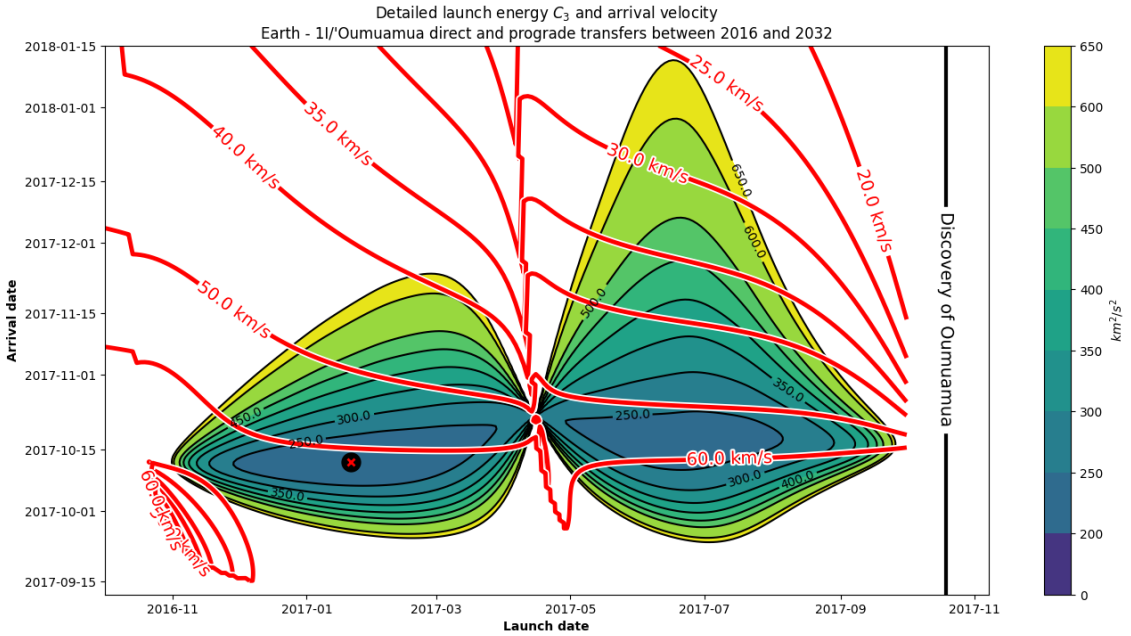


**Fig. 4.10:** Detailed porkchop showing the optimum transfer for 1I/'Oumuamua with isolines for the arrival velocity. The optimum transfer point is represented by a black dot with a red cross.

The total time of flight $\Delta t$ is 264 days. The total cost of the launch is $\Delta v_{\text{launch}} = \Delta v_e + \Delta v_1 = 11.20 + 2.96 = 14.16$ km/s. The arrival impulse is $\Delta v_2 = 62.33$ km/s. If the rendezvous is considered, the total cost of the maneuver adds up to $\Delta v = 76.49$ km/s. All

the impulses are collected in table 4.2.

| Object | Launch date | Arrival date | Required $C_3$ [km$^2$/s$^2$] |
|---|---|---|---|
| 1I/'Oumuamua | 2017-01-20 | 2017-10-12 | 200.64 |

Table 4.1: Optimum transfer orbit for a direct transfer between the Earth and 1I/'Oumuamua. The energy includes the required impulse for escaping the Earth and for performing a targeting maneuver.

Figures 4.11, 4.12, and 4.13 represent the trajectory of the optimum transfer between Earth and 1I/'Oumuamua. Note that the transfer orbit lies close to the ecliptic and has a very low inclination. This allows to take advantage of the Earth's velocity to intercept the interloper, reducing the required energy for the transfer.

| Impulse | $\Delta v_x$ [km/s] | $\Delta v_y$ [km/s] | $\Delta v_z$ [km/s] |
|---|---|---|---|
| Launch | 1.02 | -1.22 | 2.49 |
| Arrival | 58.97 | -14.18 | 14.37 |

Table 4.2: Impulses required for the optimum transfer between Earth and 1I/'Oumuamua.

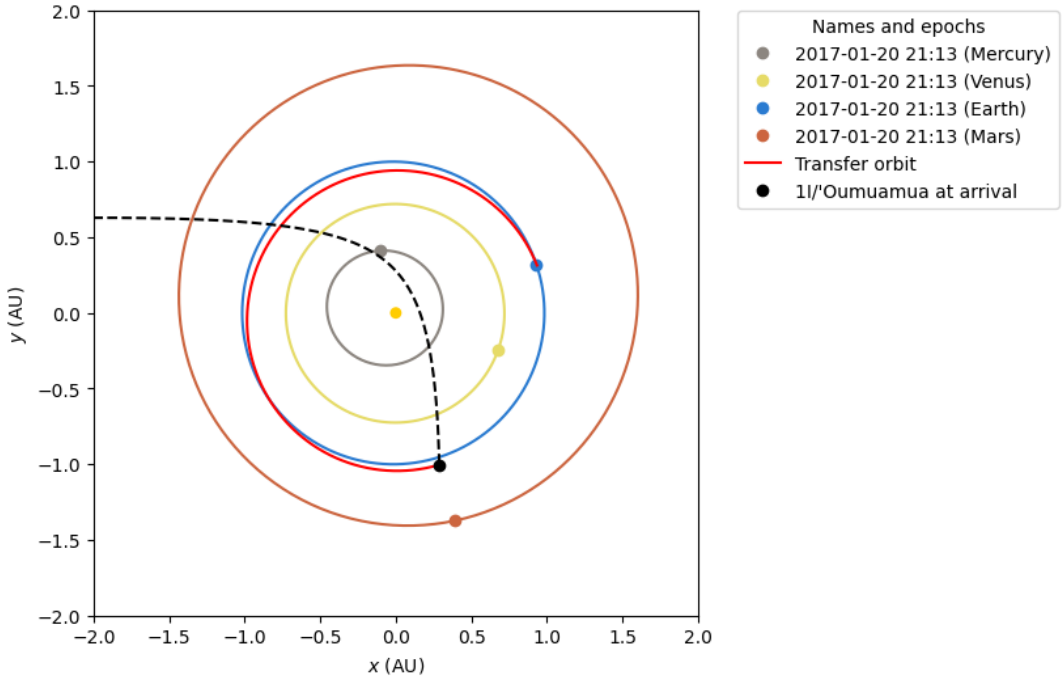


**Fig. 4.11:** Top view of the direct optimum transfer orbit from Earth to 1I/'Oumuamua. The orbit lies close to the ecliptic, taking advantage of the Earth's velocity to intercept the interloper.

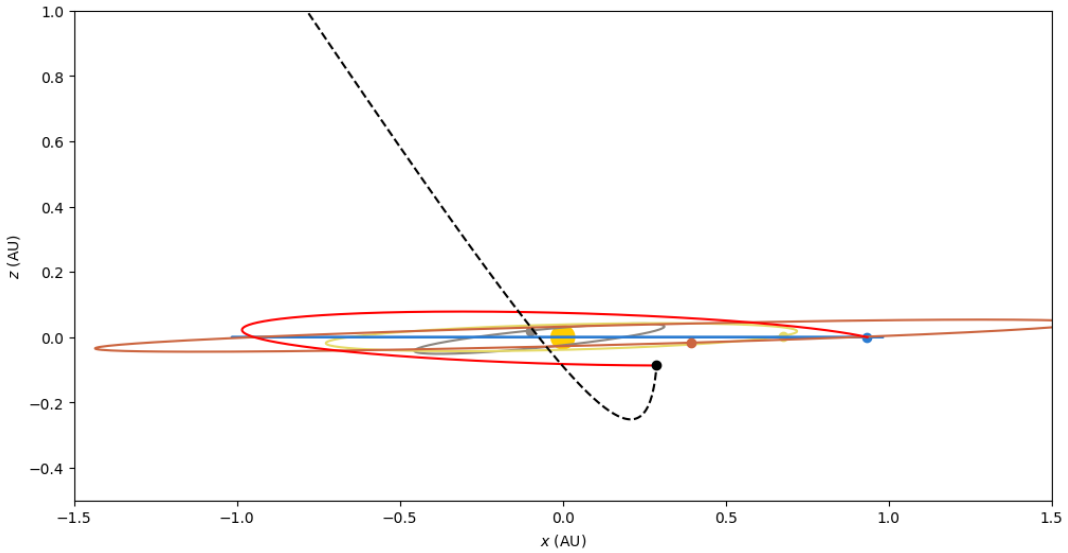


**Fig. 4.12:** Front view of the direct optimum transfer orbit from Earth to 1I/'Oumuamua. The inclination of the orbit is very low, maximizing the kinetic energy provided by the Earth. Legend shared with figure 4.11.

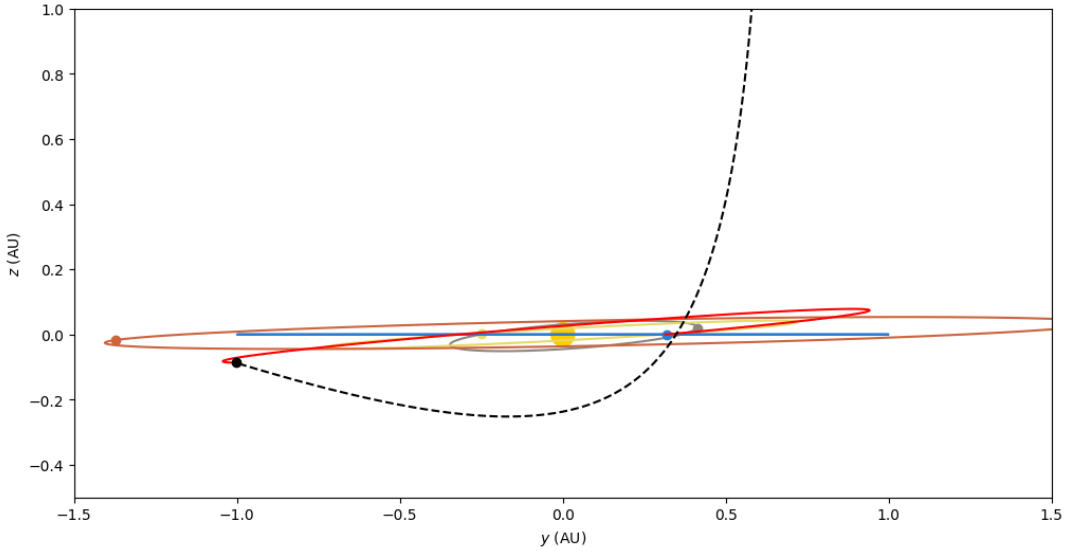


**Fig. 4.13:** Side view of the direct optimum transfer orbit from Earth to 1I/'Oumuamua. This view shows again the low inclination of the transfer orbit. Legend shared with figure 4.11.

### 4.3.2 2I/Borisov

Regarding 2I/Borisov, the most optimum transfer is also a prograde transfer. The analysis of figure 4.3 reveals a series of periodic regions in the lower left region. The region containing the lowest characteristic energy is shown in figure 4.14. The analysis is expanded again to the arrival velocity, which is shown in figure 4.15.

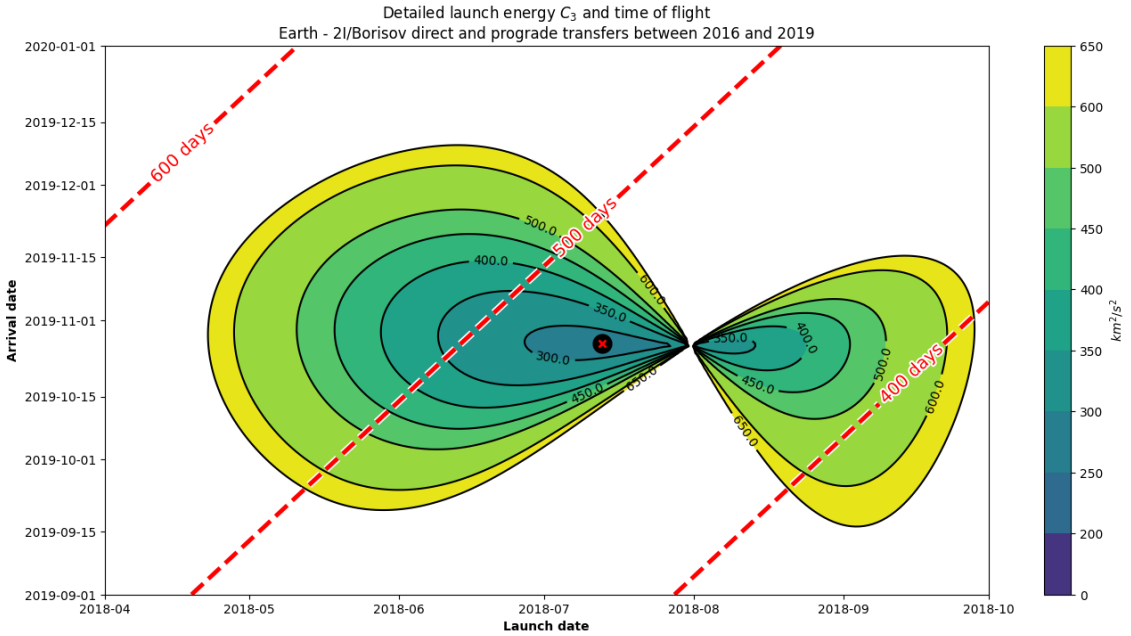


**Fig. 4.14:** Detailed porkchop showing the optimum transfer for 2I/Borisov with isolines for the time of flight. The optimum transfer point is represented by a black dot with a red cross. A region below 50 $km^2/s^2$ is found, similarly to the case of 1I/'Oumuamua.

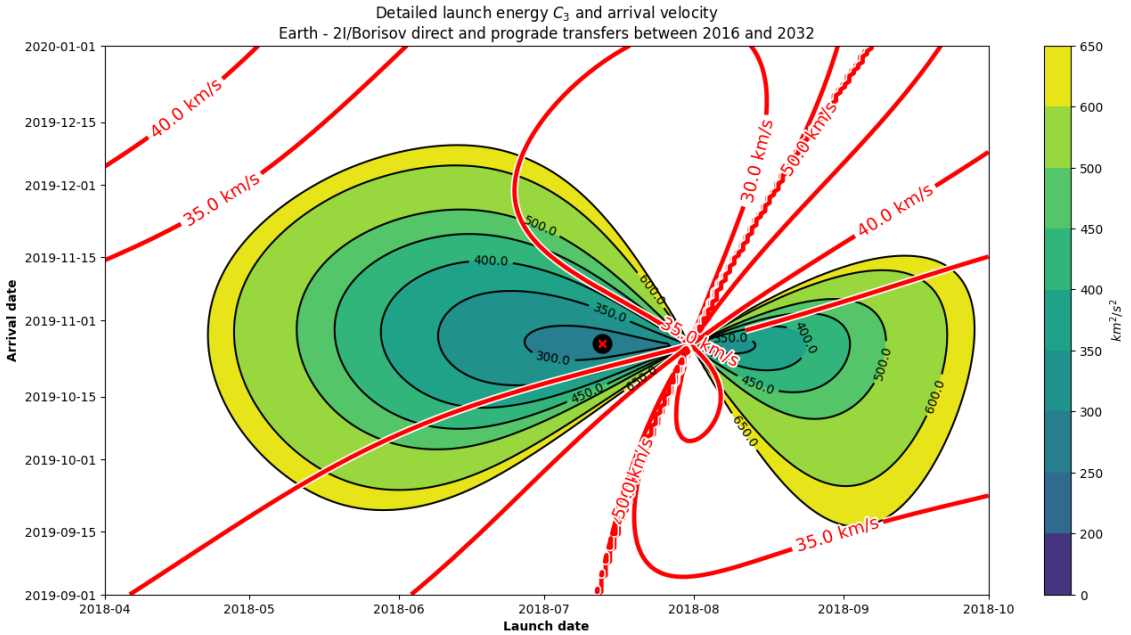


**Fig. 4.15:** Detailed porkchop showing the optimum transfer for 2I/Borisov with isolines for the arrival velocity. The optimum transfer point is represented by a black dot with a red cross. Despite having found an optimum transfer, the arrival velocity is very high.

The values associated with the point with the lowest characteristic energy for 2I/Borisov are collected in table 4.3.

| Object | Launch date | Arrival date | Required $C_3$ [km$^2$/s$^2$] |
|---|---|---|---|
| 2I/Borisov | 2018-07-12 | 2019-10-26 | 283.74 |

Table 4.3: Optimum orbit for a direct transfer between the Earth and 2I/Borisov. The enegy includes the required impulse for escaping the Earth and for performing a targeting maneuver.

The total time of flight $\Delta t$ is 470 days. The total cost of the launch is $\Delta v_{\text{launch}} = \Delta_e + \Delta v_1 = 11.20 + 5.64 = 16.86$ km/s. The arrival impulse is $\Delta v_2 = 33.00$ km/s. If the rendezvous is considered, the total cost of the maneuver adds up to $\Delta v = 49.86$ km/s. All the impulses are collected in table 4.4.

Figures 4.16, 4.17, and 4.18 represent the trajectory of the optimum transfer from Earth to 2I/Borisov. Again, the transfer does not present a high inclination, which allows the spacecraft to benefit from Earth's velocity.

| Impulse | $\Delta v_x$ [km/s] | $\Delta v_y$ [km/s] | $\Delta v_z$ [km/s] |
|---|---|---|---|
| Launch | 5.32 | 1.85 | 0.30 |
| Arrival | -1.70 | -18.30 | -27.41 |

Table 4.4: Impulses required for the optimum transfer between Earth and 2I/Borisov. These values assume that the spacecraft has already reached its escape velocity.

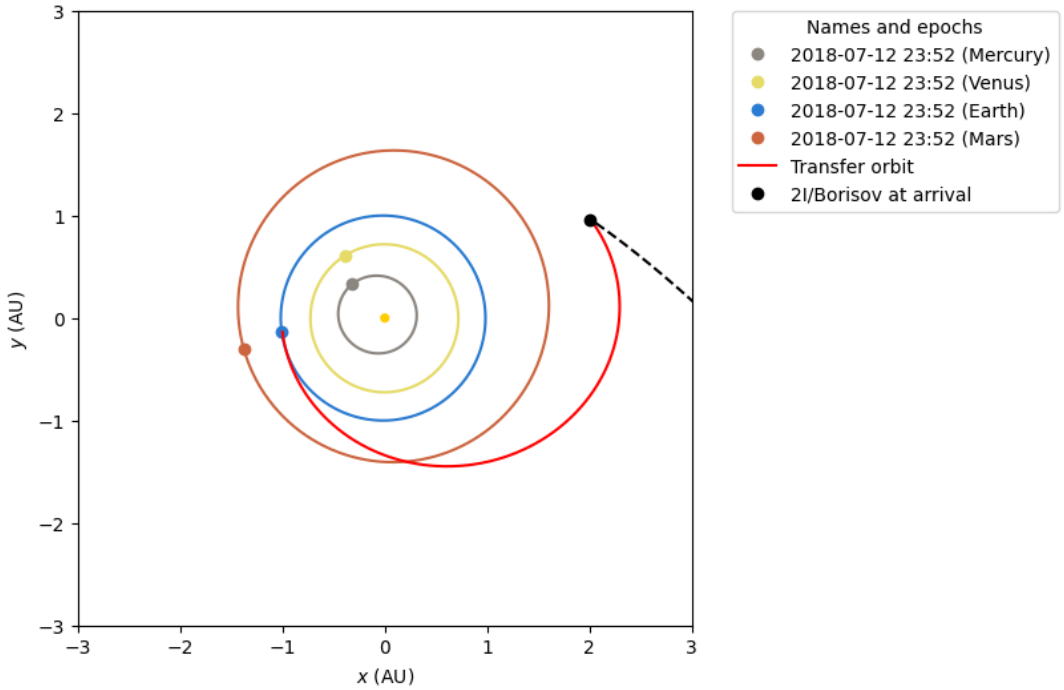


**Fig. 4.16:** Top view of the direct optimum transfer orbit from Earth to 2I/Borisov. The orbit lies close to the ecliptic, taking advantage of the Earth's velocity to intercept the interloper.

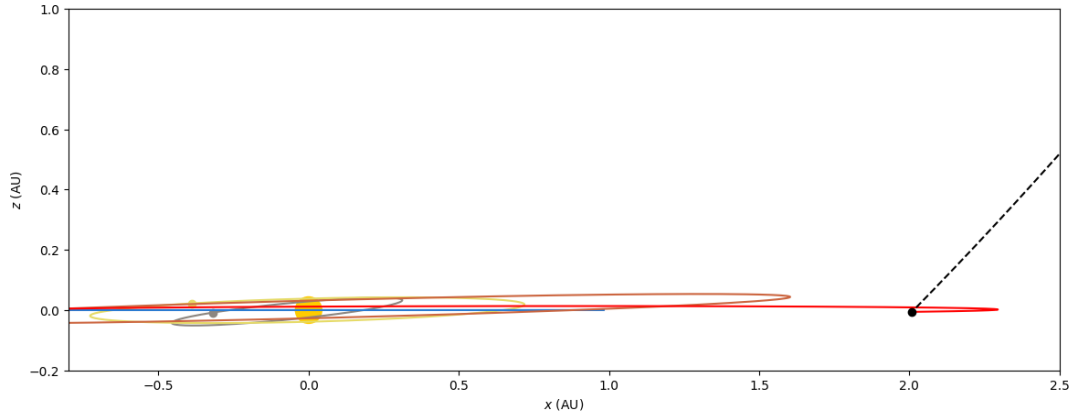


**Fig. 4.17:** Front view of the direct optimum transfer orbit from Earth to 2I/Borisov. The inclination of the orbit is very low, maximizing the kinetic energy provided by the Earth. Legend shared with figure 4.16.

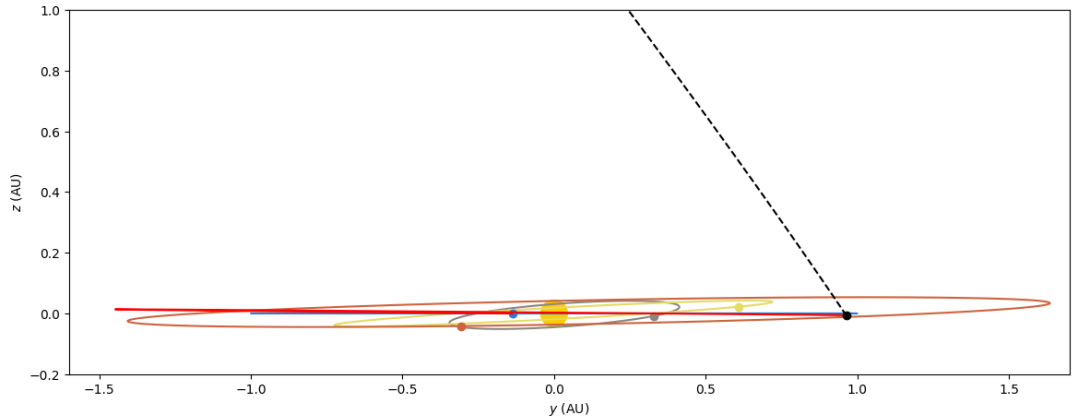


**Fig. 4.18:** Side view of the direct optimum transfer orbit from Earth to 2I/Borisov. This view shows again the low inclination of the transfer orbit. Legend shared with figure 4.16.

## 4.4 Summary

Results obtained in tables 4.2 and 4.4 show that the direct transfers require small launch impulses, once the escape velocity of Earth is overcome. However, they present large arrival velocities. This limits the amount of observation time when performing a targeting with the ISOs.

Paying attention to figures 4.13 and 4.18, it can be identified that the transfer orbits with the lowest launch energies reach the target when this is near the ecliptic.

Bibliography proofs that the optimum direct transfer for 2I/Borisov is the same as the one computed by Hibberd et al. 2021. However, the optimum direct transfer for 1I/'Oumuamua computed in this work could expand the research from Hein et al. 2018.

# 5 Alternate transfers

After the results obtained in section 4.3, it is possible now to study the possibility of using alternate transfers. The main goal of this second analysis is to find a suitable transfer that is less expensive than a direct transfer from the Earth. For this purpose, the following scenarios are considered: orbits launching from a Lagrange point and gravity assisted maneuvers.

## 5.1 Lagrange points analysis

Lagrangian points are a set of special locations in the vicinity of two massive bodies where a small object will maintain a relatively stable position relative to the two massive bodies. The five Lagrange points are labeled L1 through L5. L1, L2, and L3 are collinear with the two massive bodies, while L4 and L5 are located at the vertices of the equilateral triangle formed by the two massive bodies. The L1, L2, and L3 points are unstable, while L4 and L5 are stable. The L4 and L5 points are sometimes called Trojan points, and the two massive bodies are sometimes called the primaries. Figure 5.1 shows the Lagrange points in the Sun - Earth-Moon barycenter system.

Despite L1, L2, and L3 being unstable, they are of particular interest because of their proximity to the primaries. In fact, stable orbits can be achieved by performing small corrections to the spacecrafts's position. Also, these points are not populated with asteroids like L4 and L5, making them excellent for long term missions.

In this work, only the point L2 belonging to the Sun - Earth system is considered. The reason for choosing this point is that it is a popular point chosed by different missions and thus, a well known point. It provides a great viewpoint. In fact, this point has been selected for other missions including the James Webb Space Telescope, see Gardner et al. 2006, or the future Comet Interceptor, see G. H. Jones et al. 2024.

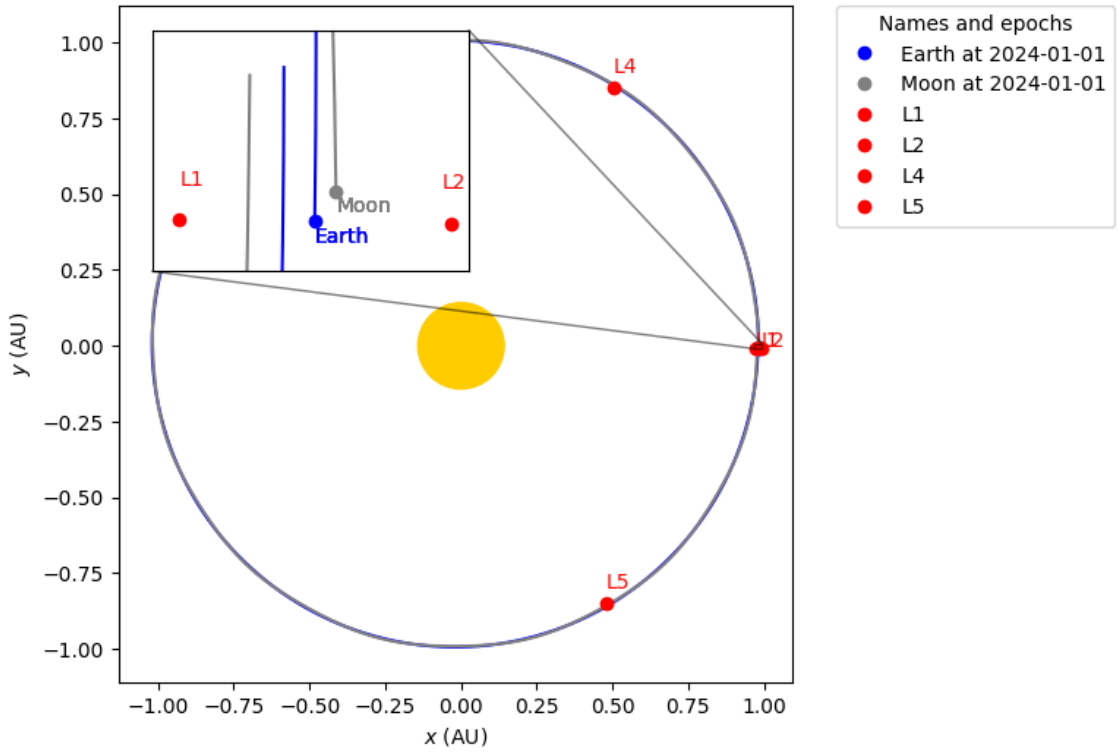


**Fig. 5.1:** Lagrange points in the Sun - Earth-Moon barycenter system. All points are shown except L3. Ephemerides for this point are not provided by the JPL Horizons system. Despite this situation, the point is not analyzed in this work. Sun is not scaled for visualization purposes.

### 5.1.1 Escape velocity from L2

For the computation of the escape velocity in the vicinity of the Lagrange points, the gravitation effects of the Earth and the Moon are considered. Even if the Lagrange points only appear in the restricted three-body problem, computing the escape velocity requires using the two-body problem is still a valid approach as long as the barycenter of the Earth-Moon system is used.

Thus, the escape velocity can be computed using equation 5.1.

$$v_{\text{esc}} = \sqrt{\frac{2\mu}{d}} = \sqrt{\frac{2\mu}{\|\vec{r_b} - \vec{r}\|}} \tag{5.1}$$

where in $\mu$ is the gravitational parameter of the Earth-Moon system, and $d$ is the distance from the point of interest to the barycenter of the Earth-Moon system, which can be computed using equation 5.2.

$$\vec{r_b} = \frac{\vec{r_\oplus} \cdot m_\oplus + \vec{r_\leftmoon} \cdot m_\leftmoon}{m_\oplus + m_\leftmoon} \tag{5.2}$$

To simplify the computer routines, an average value for the escape velocity has been computed by solving previous equations for a span of time ranging between years 2000 and 2050. The mean value for the escape velocity from L2 is 0.73 km/s.

### 5.1.2 Optimum direct transfers from L2

The analysis for a direct optimum transfer from L2 to each one of the discovered ISOs follows the same model than the one presented in chapter 4.

#### 1I/'Oumuamua

Figures 5.2 and 5.3 show the porkchop plots showing the launch energy, time of flight, and arrival velocity for a direct prograde launch between L2 and 1I/'Oumuamua.

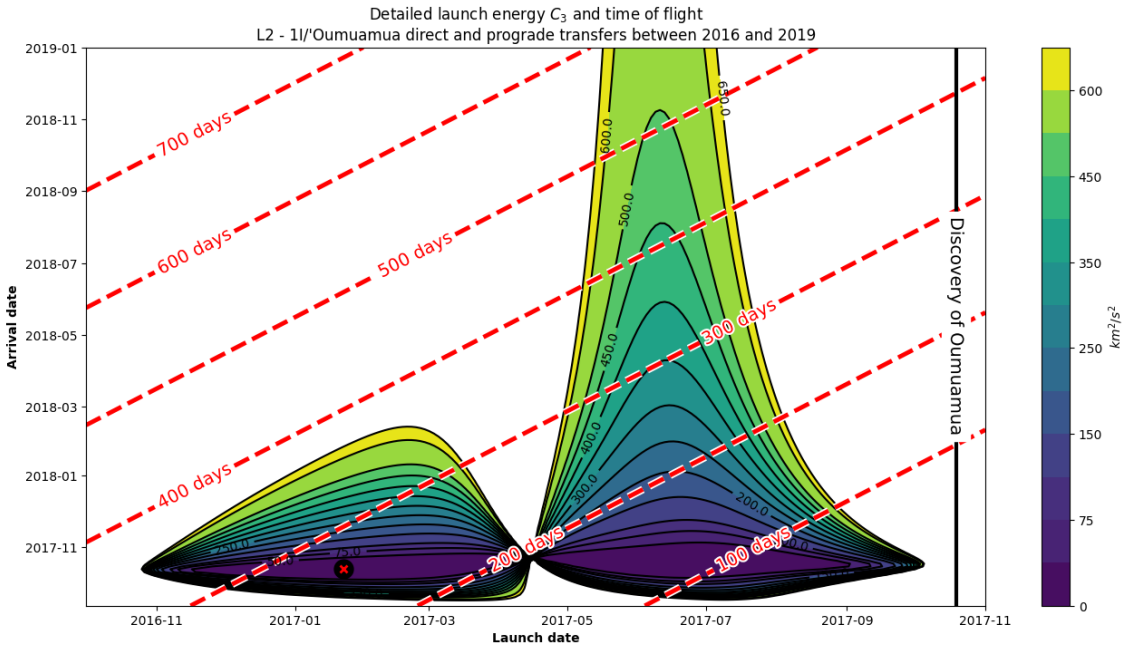


**Fig. 5.2:** Detailed porkchop showing the optimum transfer for L2 to 1I/'Oumuamua. The optimum transfer point is represented by a black dot with a red cross.

Note that these figures are very similar to the ones in 4.9 and 4.10. The main difference is that launching from L2 requires less fuel, since the escape velocity is lower. The required launch energy reduces about 92.81%. Despite this advantage, the arrival velocity is still high. Launch and arrival dates are shown in table 5.1.

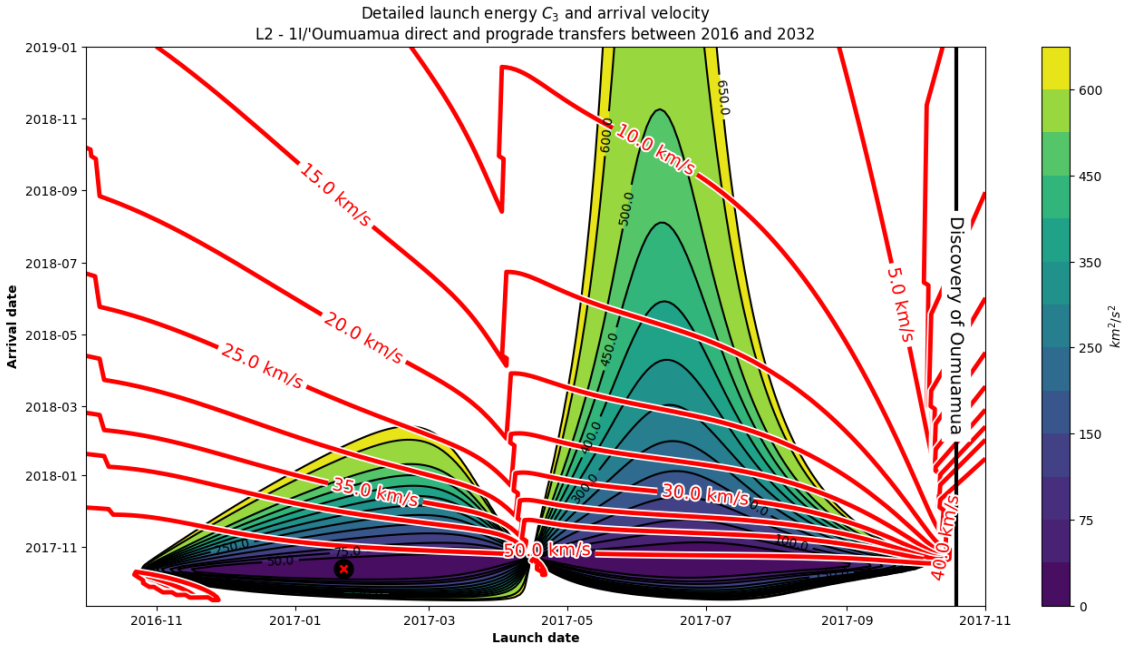


**Fig. 5.3:** Detailed porkchop showing the optimum transfer for L2 to 1I/'Oumuamua with isolines for the arrival velocity. The optimum transfer point is represented by a black dot with a red cross.

| Object | Launch date | Arrival date | Required $C_3$ [km$^2$/s$^2$] |
|---|---|---|---|
| 1I/'Oumuamua | 2017-01-22 | 2017-10-13 | 14.41 |

Table 5.1: Optimum transfer orbit for a direct transfer between L2 and 1I/'Oumuamua. The energy includes the required impulse for escaping the L2 point and for performing a targeting maneuver.

The optimum transfer orbit is found to have a time of flight $\Delta t = 263.67$ days. The total cost of the launch is $\Delta v_{\text{launch}} = \Delta v_e + \Delta v_1 = 0.73$ km/s $+ 3.07$ km/s $= 3.80$ km/s. The arrival impulse is $\Delta v_2 = 61.46$ km/s. If the rendezvous is considered, the total cost of the maneuver adds up to $\Delta v = 64.53$ km/s. Detailed impulses are shown in table 5.2.

| Impulse | $\Delta v_x$ [km/s] | $\Delta v_y$ [km/s] | $\Delta v_z$ [km/s] |
|---|---|---|---|
| Launch | 1.67 | -1.30 | 2.21 |
| Arrival | 58.04 | -14.06 | 14.47 |

Table 5.2: Required impulses for a direct prograde transfer between L2 and 1I/'Oumuamua.

### 2I/Borisov

Figures 5.4 and 5.5 show the porkchop plots showing the launch energy, time of flight, and arrival velocity for a direct prograde launch between L2 and 2I/Borisov.

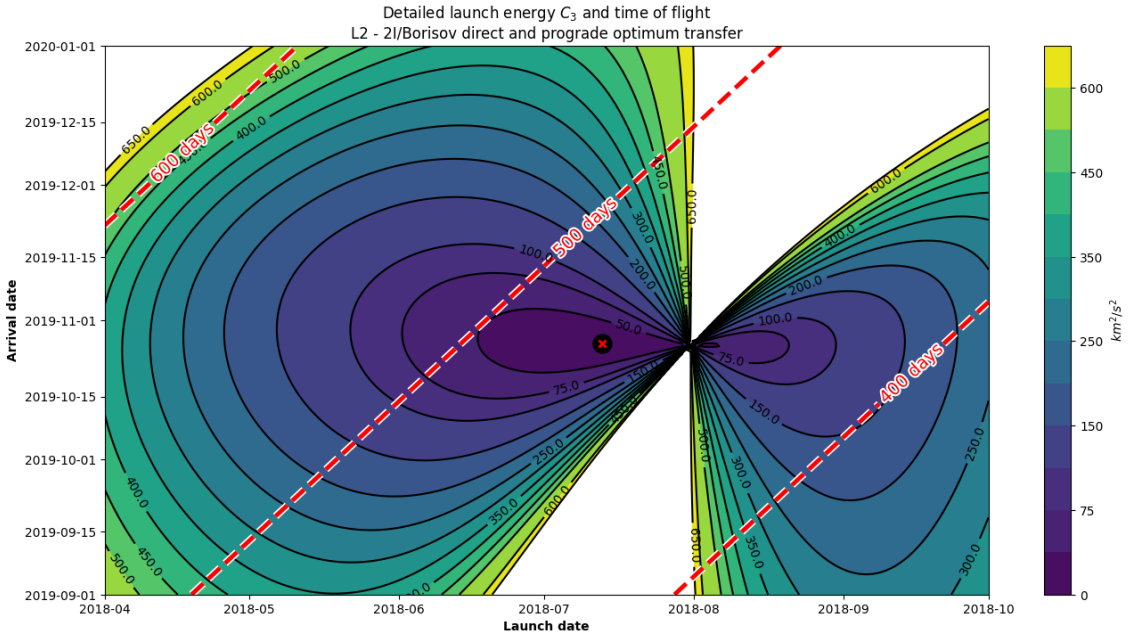


**Fig. 5.4:** Detailed porkchop showing the optimum transfer for L2 to 2I/Borisov. The optimum transfer point is represented by a black dot with a red cross. A point under 50 $km^2/s^2$ is found, highly reducing the launch cost from this Lagrange point.

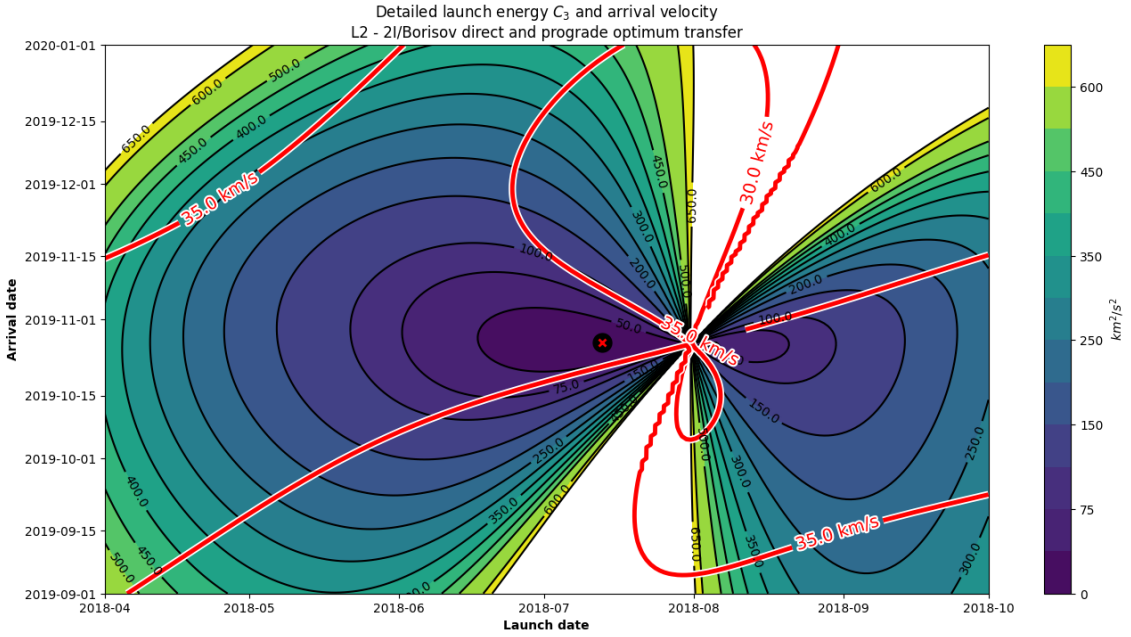


**Fig. 5.5:** Detailed porkchop showing the optimum transfer for L2 to 2I/Borisov with isolines for the arrival velocity. The optimum transfer point is found to have an arrival speed close to 33 km/s. The optimum transfer point is represented by a black dot with a red cross.

Again, these figures are very similar to the ones in 4.14 and 4.15. Again, launching from L2 requires less fuel. The required launch energy reduces about 88.08%, yet the arrival velocity is still high. Launch and arrival dates are shown in table 5.3.

| Object | Launch date | Arrival date | Required $C_3$ [km$^2$/s$^2$] |
|---|---|---|---|
| 2I/Borisov | 2018-07-12 | 2019-10-26 | 34.30 |

Table 5.3: Optimum transfer orbit for a direct transfer between L2 and 2I/Borisov. The energy includes the required impulse for escaping the L2 point and for performing a targeting maneuver.

The optimum transfer orbit is found to have a time of flight $\Delta t = 470.79$ days. The total cost of the launch is $\Delta v_{\text{launch}} = \Delta v_e + \Delta v_1 = 0.73$ km/s $+ 5.13$ km/s $= 5.83$ km/s. The arrival impulse is $\Delta v_2 = 33.02$ km/s. If the rendezvous is considered, the total cost of the maneuver adds up to $\Delta v = 38.85$ km/s. Detailed impulses are shown in table 5.3.

| Impulse | $\Delta v_x$ [km/s] | $\Delta v_y$ [km/s] | $\Delta v_z$ [km/s] |
|---|---|---|---|
| Launch | 4.82 | 1.71 | 0.30 |
| Arrival | -1.61 | -18.34 | -27.42 |

Table 5.4: Required impulses for a direct prograde transfer between L2 and 2I/Borisov.

#### Summary

Results obtained for the direct transfers from L2 to 1I/'Oumuamua and 2I/Borisov not only demonstrate significant reductions in launch energy but also underscore the strategic advantage of positioning a spacecraft at the Lagrange point L2. By parking a spacecraft at L2, the mission can leverage its stable orbit and gravitational equilibrium, effectively establishing a strategic vantage point for interstellar rendezvous. This positioning provides invaluable reaction time, enabling meticulous planning and adjustment of trajectory parameters before initiating the final approach toward the target object.

## 5.2 Gravity assist analysis

Gravity assists are a well-known maneuver for changing the velocity of a spacecraft by using the gravitational pull of a planet. The spacecraft flies by the planet and gains or loses velocity depending on the relative motion of the planet and the spacecraft. This technique is used to save fuel and time, and is commonly used in interplanetary missions.

Flandro 1966 makes a great introduction about the basics of gravity assists that lead to the development of missions like Voyayer I and Voyayer II.

This analysis only considers unpowered gravity assists, in which the spacecraft does not lose mass or performs any propulsive maneuvers.

The characteristic energy of a spacecraft in the heliocentric frame is given by equation 5.3:

$$E_s = \frac{1}{2}V_s^2 \tag{5.3}$$

where $V_s$ is the velocity of the spacecraft in the heliocentric frame.

Consider a planet moving at a speed of $V_p$ in the heliocentric frame. Assuming a spacecraft approaches the planet with a speed of $\vec{v}_{\text{in},\infty}$ and that it leaves the planet with a speed of $\vec{v}_{\text{out},\infty}$, both as seen by the planet. From the point of view of the planet, $v_{\text{in},\infty} = v_{\text{out},\infty} = v_\infty$. Despite their modulus being the same, the direction of these vectors is different. Thus, $\vec{v}_{\text{in},\infty} \neq \vec{v}_{\text{out},\infty}$.

From the heliocentric perspective, the spacecraft approaches the planet with a velocity $\vec{V}_{\text{in}} = \vec{V}_p + \vec{v}_{\text{in},\infty}$ and leaves the planet with a velocity $\vec{V}_{\text{out}} = V_p + \vec{v}_{\text{out},\infty}$.

The angle between $\vec{v}_{\text{in},\infty}$ and $\vec{v}_{\text{out},\infty}$ is known as the deflection angle, $\psi$. The speed $v)\infty$ and the maximum $\psi$ are related once the altitude $h = d - R_p$ of the flyby is set, being $R_p$ the radius of the planet. This relation is exposed by equation 5.4:

$$\psi_{\max} = 2 \cdot \arcsin\left(\frac{\mu}{\mu + v_\infty^2(R_p + h)}\right) \tag{5.4}$$

Figure 5.6 is generated by solving equation 5.4 at an altitude of $h = R_p$ for different values of $v_\infty$ at each planet of the solar system.

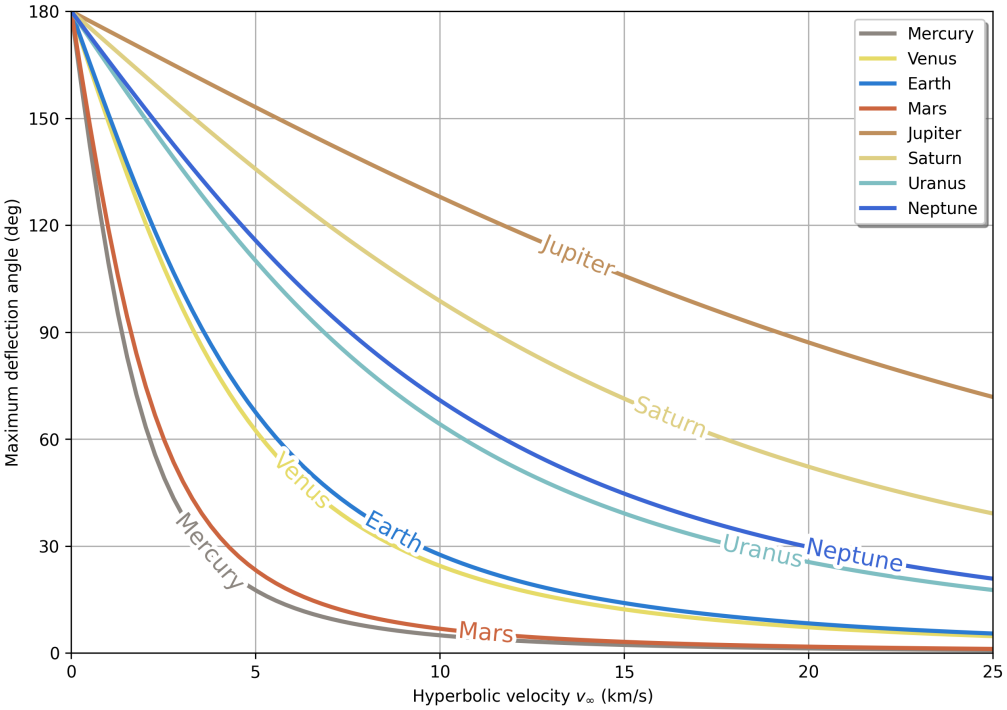


**Fig. 5.6:** Maximum deflection angle as a function of the speed of the spacecraft at different planets. Flyby altitude is $h = R_p$.

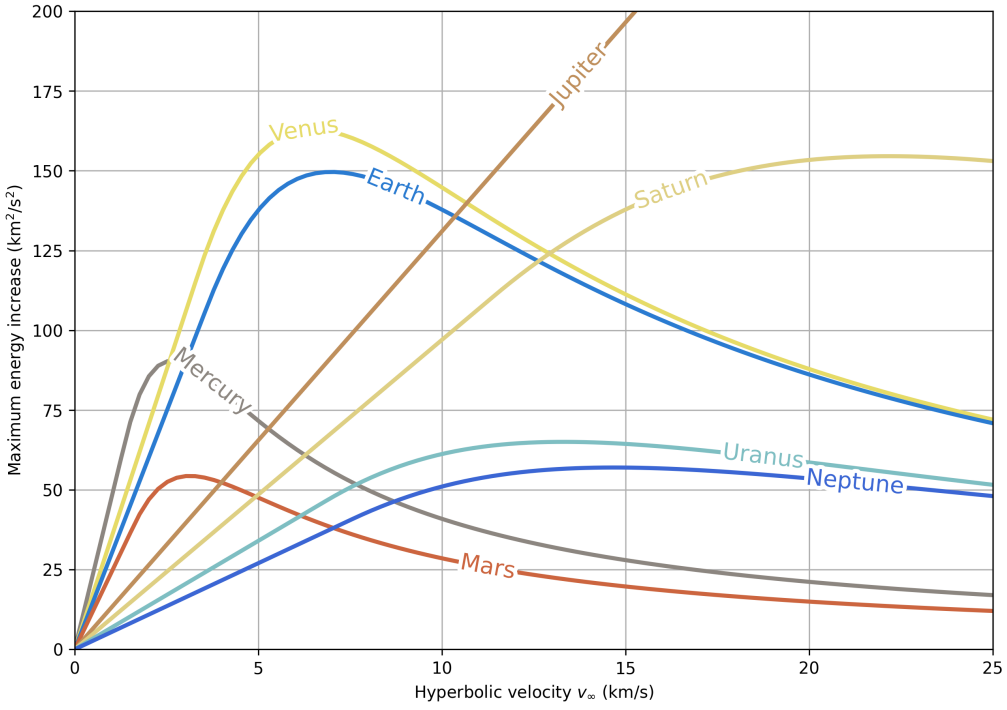


**Fig. 5.7:** Maximum energy increment as a function of the speed of the spacecraft at different planets. Evaluated at the maximum deflection angle. Mean values for planetary orbital speed were used.

Looking at figure 5.6, one could think that Jupiter woudl provide the highest increments in the characteristic energy since it provides the highest deflection angle for a given hyperbolic speed. However, figure 5.7 shows that the maximum energy increment depends on the planet.

The relationship between the increment in the characteristic energy and the hyperbolic speed is not linear and is given by equation 5.5:

$$\Delta E = f_{\max} E^* = f_{\max} V_p v_\infty \tag{5.5}$$

where $f_{\max}$ is the maximum energy increment factor given by equation 5.6:

$$f_{\max} = \begin{cases} \frac{\cos\epsilon + 1}{2} & \text{if } \epsilon \geq \pi - \psi_{\max} \\ \frac{\cos\epsilon - \cos(\psi_{\max} + \epsilon)}{2} & \text{otherwise} \end{cases} \tag{5.6}$$

where $\epsilon$ is the angle between the direction of the asymptote and the planet's velocity vector.

Note that for a certain hyperbolic speed, the maximum energy other planets rather than Jupiter may provide higher energy increments. For example, below $v_\infty < 10$ km/s, Venus and Earth are more efficient than Jupiter for $\psi_{\max}$. The same happens for Mercury at $v_{\max} < 5.00$ km/s.

Despite this analysis, it is important to note that the energy increment does not always take place at the maximum deflection angle. The orientation of the incoming hyperbolic speed vector and its magnitude will determine the state after the gravity assist. In fact, it may be possible that a gravity assist is not beneficial at all, requiring more fuel to insert the spacecraft into the right flyby trajectory and incresing the time of flight of the mission.

Computation for the most optimum transfers between L2 and inner planets show that for the case of 1I/'Oumuamua and 2I/Borisov, performing an impulse to any near planet already requires more energy than the one for a direct transfer to the interloper.

# 6 Conclusions

After the direct transfer analysis from Earth in 4, the direct transfer analysis from L2 in 5.1, and a the gravity assist review in 5.2, this chapter sumarizes all the results and presents the final conclusions.

## 6.1 Optimum direct transfer: Earth vs L2

Results for the optimum direct transfer computed previous chapters are summarized in tables 6.1, 6.2 and 6.3. A high reduction in the launch energy is observed when launching from L2 instead of Earth. This reduction is mainly due to the low escape velocity at L2, which allows for a more efficient transfer.

| Object | $\Delta v$ launch Earth [km/s] | $\Delta v$ launch L2 [km/s] | Reduction [%] |
|---|---|---|---|
| 1I/'Oumuamua | 13.85 | 3.80 | 72.56 |
| 2I/Borisov | 16.90 | 5.85 | 65.38 |

Table 6.1: Comparison of the launch velocity for direct transfers from Earth and L2. These values are feasible considering modern propulsion technology, see Longhurst 2021.

| Object | $C_3$ launch Earth [km$^2$/s$^2$] | $C_3$ launch L2 [km$^2$/s$^2$] | Reduction [%] |
|---|---|---|---|
| 1I/'Oumuamua | 192.00 | 14.41 | 92.51 |
| 2I/Borisov | 286.00 | 34.30 | 88.08 |

Table 6.2: Comparison of the launch energy for direct transfers from Earth and L2. A reduction in energy is observed when launching from L2.

| Object | $\Delta V$ arrival Earth [km/s] | $\Delta V$ arrival L2 [km/s] | Reduction [%] |
|---|---|---|---|
| 1I/'Oumuamua | 62.33 | 61.46 | 1.40 |
| 2I/Borisov | 33.00 | 33.02 | -0.06 |

Table 6.3: Comparison of the arrival velocity for direct transfers from Earth and L2. Due to the close proximity of L2 to the Earth, the reduction in arrival speed is low compared to the reduction in launch energy.

Note that the required $\Delta v$ values for a transfer originating at L2 can be achieved with modern propulsion technology and gravitational assists. However, this research considers the usage of impulsive maneuvers, that is, maneuvers that occur instantaneously. In reality, the spacecraft would need to perform a maneuver over a period of time. Not only this, figure 3.2 only considers main space launchers, which are used for launching satellites.

For a spacecraft placed at L2, a bipropellant chemical propulsion system, such as one using liquid oxygen and liquid hydrogen or liquid oxygen and liquid ethanol, would be a feasible option to provide the required 3.5 km/s of $\Delta v$. The high specific impulse of bipropellant systems makes them capable of delivering this level of performance.

Leveraging the advantageous position of L2 not only facilitates spacecraft parking while awaiting the discovery of new ISOs but also augments mission adaptability. By pre-positioning a spacecraft in space, it affords greater maneuverability and flexibility in mission planning. This positioning grants extended reaction time, enabling meticulous mission strategizing and the optimization of trajectory paths.

Tables 6.4 and 6.5 summary the optimum launch dates for 1I/'Oumuamua and 2I/Borisov, respectively. It is worth mentioning that the optimum launch dates for 1I/'Oumuamua and 2I/Borisov take place before humanity discovered them. This fact highlights the importance of increasing the investment in space surveillance and tracking systems. By doing so, the reaction time to intercept an ISO could be reduced significantly, allowing for more efficient missions.

| Object | Optimum date launch Earth | Optimum date launch L2 | Discovery date |
|---|---|---|---|
| 1I/'Oumuamua | 2017-01-20 | 2017-01-22 | 2017-10-19 |

Table 6.4: Optimum launch dates for 1I/'Oumuamua compared to its discovery date. The first interstellar interloper was discovered close to 270 days after an optimum transfer could have been launched from Earth or L2.

| Object | Optimum date launch Earth | Optimum date launch L2 | Discovery date |
|---|---|---|---|
| 2I/Borisov | 2018-07-12 | 2018-07-12 | 2019-08-30 |

Table 6.5: Optimum launch dates for 2I/Borisov compared to its discovery date. The second interstellar interloper was discovered close to 414 days after an optimum transfer could have been launched from Earth or L2.

## 6.2 About gravity assists

Regarding the analysis of gravity assists, it is determined that their feasibility hinges on several factors. These encompass the relative spatial configurations of planets during the launch phase, the duration of the mission, the inclination concerning the ecliptic plane of the ISO, the velocity of the interloper, and the launch velocity itself. In scenarios ripe with optimism, the feasibility of executing multiple gravity assists, possibly involving inner planets, emerges as a promising prospect.

These results mirror the strategic approach undertaken by the Comet Interceptor mission. The mission advocates for the adoption of a direct external transfer orbit from L2 in a ready-to-launch state to the interloper, presenting it as an initial solution to surmount the intricacies associated with interplanetary transfer challenges.

## 6.3 Future work

While working on this project, the author noticed a lack of robust software for optimizing gravity assist trajectories. Trajectory optimization in astrodynamics is complex, especially when dealing with multiple planetary flybys and impulsive maneuvers.

Creating software to optimize gravity assist trajectories considering variables like planetary configurations, time spans, and fuel constraints would be highly beneficial. Such software could quickly design an optimal mission to intercept an interstellar visitor, helping astrodynamicists overcome challenges like high relative speeds and inclinations.

# Bibliography


Bodewits, D., Noonan, J. W., Feldman, P. D., Bannister, M. T., Farnocchia, D., Harris, W. M., Li, J.-Y., Mandt, K. E., Parker, J. W., & Xing, Z.-X. (2020). The carbon monoxide-rich interstellar comet 2i/borisov. *Nature Astronomy*, *4*(9), 867–871. https://doi.org/10.1038/s41550-020-1095-2

Daly, R. T., Ernst, C. M., Barnouin, O. S., Chabot, N. L., Rivkin, A. S., Cheng, A. F., Adams, E. Y., Agrusa, H. F., Abel, E. D., Alford, A. L., Asphaug, E. I., Atchison, J. A., Badger, A. R., Baki, P., Ballouz, R.-L., Bekker, D. L., Bellerose, J., Bhaskaran, S., Buratti, B. J., … Zhang, Y. (2023). Successful kinetic impact into an asteroid for planetary defence. *Nature*, *616*(7957), 443–447. https://doi.org/10.1038/s41586-023-05810-5

Dehnen, W., & Binney, J. J. (1998). Local stellar kinematics from Hipparcos data. *Monthly Notices of the Royal Astronomical Society*, *298*(2), 387–394. https://doi.org/10.1046/j.1365-8711.1998.01600.x

Do, A., Tucker, M. A., & Tonry, J. (2018). Interstellar Interlopers: Number Density and Origin of ‘Oumuamua-like Objects. *The Astrophysical Journal Letters*, *855*(1), Article L10, L10. https://doi.org/10.3847/2041-8213/aaae67

Feng, F., & Jones, H. R. A. (2018). ’oumuamua as a messenger from the local association. *The Astrophysical Journal Letters*, *852*(2), Article L27, L27. https://doi.org/10.3847/2041-8213/aaa404

Flandro, G. (1966). Fast reconnaissance missions to the outer solar system aiaa-2000-3334. dover, ny (197 1). utilizing energy derived from the gravitational field of jupiter. *Astronautica Acta*, 12–329.

Fouchard, M., Rickman, H., Froeschlé, C., & Valsecchi, G. B. (2011). The last revolution of new comets: The role of stars and their detectability. *A&A*, *535*, A86. https://doi.org/10.1051/0004-6361/201116514

Francis, P. J. (2005). The demographics of long-period comets. *The Astrophysical Journal*, *635*(2), 1348–1361. https://doi.org/10.1086/497684

Fraser, W. C., Pravec, P., Fitzsimmons, A., Lacerda, P., Bannister, M. T., Snodgrass, C., & Smolić, I. (2018). The tumbling rotational state of 1i/‘oumuamua. *Nature Astronomy*, *2*(5), 383–386. https://doi.org/10.1038/s41550-018-0398-z

Gaidos, E., Williams, J., & Kraus, A. (2017). Origin of interstellar object a/2017 u1 in a nearby young stellar association? *Research Notes of the AAS*, *1*(1), 13. https://doi.org/10.3847/2515-5172/aa9851

Gardner, J. P., Mather, J. C., Clampin, M., Doyon, R., Greenhouse, M. A., Hammel, H. B., Hutchings, J. B., Jakobsen, P., Lilly, S. J., Long, K. S., Lunine, J. I., Mccaughrean, M. J., Mountain, M., Nella, J., Rieke, G. H., Rieke, M. J., Rix, H.-W., Smith, E. P., Sonneborn, G., … Wright, G. S. (2006). The james webb space telescope. *Space Science Reviews*, *123*(4), 485–606. https://doi.org/10.1007/s11214-006-8315-7

Hein, A. M., Perakis, N., Eubanks, T. M., Hibberd, A., Crowl, A., Hayward, K., au2, R. G. K. I., & Osborne, R. (2018). Project lyra: Sending a spacecraft to 1i/'oumuamua (former a/2017 u1), the interstellar asteroid.

Hibberd, A., Perakis, N., & Hein, A. M. (2021). Sending a spacecraft to interstellar comet 2i/borisov.

Higuchi, A., & Kokubo, E. (2019). Hyperbolic orbits in the Solar system: interstellar origin or perturbed Oort cloud comets? *Monthly Notices of the Royal Astronomical Society*, *492*(1), 268–275. https://doi.org/10.1093/mnras/stz3153

Horner, J., Evans, N. W., Bailey, M. E., & Asher, D. J. (2003). The populations of comet-like bodies in the Solar system. *Monthly Notices of the Royal Astronomical Society*, *343*(4), 1057–1066. https://doi.org/10.1046/j.1365-8711.2003.06714.x

Izzo, D. (2014). Revisiting lambert's problem. *Celestial Mechanics and Dynamical Astronomy*, *121*(1), 1–15. https://doi.org/10.1007/s10569-014-9587-y

Jewitt, D., Hui, M.-T., Kim, Y., Mutchler, M., Weaver, H., & Agarwal, J. (2020). The nucleus of interstellar comet 2i/borisov. *The Astrophysical Journal Letters*, *888*(2), L23. https://doi.org/10.3847/2041-8213/ab621b

Jewitt, D., Luu, J., Rajagopal, J., Kotulla, R., Ridgway, S., Liu, W., & Augusteijn, T. (2017). Interstellar interloper 1i/2017 u1: Observations from the not and wiyn telescopes. *The Astrophysical Journal Letters*, *850*(2), L36. https://doi.org/10.3847/2041-8213/aa9b2f

Jewitt, D., & Seligman, D. (2023). The interstellar interlopers. *61*, 197–236. https://doi.org/10.1146/annurev-astro-071221-054221

Jones, G. H., Snodgrass, C., Tubiana, C., Küppers, M., Kawakita, H., Lara, L. M., Agarwal, J., André, N., Attree, N., Auster, U., Bagnulo, S., Bannister, M., Beth, A., Bowles, N., Coates, A., Colangeli, L., Corral van Damme, C., Da Deppo, V., De Keyser, J., … Ji, H. (2024). The comet interceptor mission. *Space Science Reviews*, *220*(1), Article 9, 9. https://doi.org/10.1007/s11214-023-01035-0

Longhurst, S. (2021). Delta-v requirements for interplanetary micro-spacecraft. https://doi.org/10.13140/RG.2.2.19781.78564

Mamajek, E. (2017). Kinematics of the Interstellar Vagabond 1I/'Oumuamua (A/2017 U1). *Research Notes of the American Astronomical Society*, *1*(1), Article 21, 21. https://doi.org/10.3847/2515-5172/aa9bdc

Marčeta, D. (2023). Synthetic population of interstellar objects in the solar system. *Astronomy and Computing*, *42*, 100690. https://doi.org/https://doi.org/10.1016/j.ascom.2023.100690

Martinez, J., & Sanjurjo, M. (2021). *Lambert's problem algorithms: A critical review*. Retrieved April 26, 2024, from https://github.com/jorgepiloto/lamberthub/blob/main/art/thesis_jorge.pdf

Mashchenko, S. (2019). Modelling the light curve of 'Oumuamua: evidence for torque and disc-like shape. *Monthly Notices of the Royal Astronomical Society*, *489*(3), 3003–3021. https://doi.org/10.1093/mnras/stz2380

Moro-Martín, A. (2023). Interstellar planetesimals. In *Planetary systems now* (pp. 333–379). World Scientific.

Napier, K. J., Adams, F. C., & Batygin, K. (2021). On the capture of interstellar objects by our solar system. *The Planetary Science Journal*, *2*(2), 53. https://doi.org/10.3847/PSJ/abe76e/53

Peña-Asensio, E., Trigo-Rodríguez, J. M., & Rimola, A. (2022). Orbital characterization of superbolides observed from space: Dynamical association with near-earth objects, meteoroid streams, and identification of hyperbolic meteoroids. *The Astronomical Journal*, *164*(3), 76. https://doi.org/10.3847/1538-3881/ac75d2

Peña-Asensio, E., Visuri, J., Trigo-Rodríguez, J. M., Socas-Navarro, H., Gritsevich, M., Siljama, M., & Rimola, A. (2024). Oort cloud perturbations as a source of hyperbolic earth impactors. *Icarus*, *408*, 115844. https://doi.org/https://doi.org/10.1016/j.icarus.2023.115844

Portegies Zwart, S., Torres, S., Pelupessy, I., Bédorf, J., & Cai, M. X. (2018). The origin of interstellar asteroidal objects like 1i/2017 u1 'oumuamua. *Monthly Notices of the Royal Astronomical Society: Letters*, *479*(1), L17–L22. https://doi.org/10.1093/mnrasl/sly088

Siraj, A., & Loeb, A. (2022). A meteor of apparent interstellar origin in the cneos fireball catalog. *The Astrophysical Journal*, *939*(1), 53. https://doi.org/10.3847/1538-4357/ac8eac

Wertz, J., Everett, D., & Puschell, J. (2011). *Space mission engineering: The new smad*. Microcosm Press. https://books.google.es/books?id=VmQmtwAACAAJ